Solution of the wave equations for a cylindrical whistler duct

Paul M. Bellan[1, a)]

Applied Physics and Materials Science, Caltech, Pasadena CA 91125, USA

(Dated: 21 November 2025)

The coupled equations governing whistler waves propagating along a duct with cylindrical cross section are derived and then solved numerically. These equations are expressed in terms of magnetic and current flux functions and show that it is possible to have a solution where the waves are finite in the duct and decay exponentially outside the duct. This solution has the property of having zero radial Poynting flux everywhere so, as required for whistler waves to bounce back and forth losslessly between magnetically conjugate terrestrial hemispheres, no wave power leaks from the duct. The coupled equations are solved numerically for a tangible realistic situation by dividing the radial domain into an inner and an outer region where the interface between these regions is at a mode conversion location where fast and slow modes inside the duct merge and effectively reflect. The result of this effective reflection is that there are fast and slow standing waves in the duct. In the region external to the duct, the wave solutions are also a form of standing waves, but with a strong exponential decay and a radial wavelength that is intermediate between that of the fast and slow waves in the duct. The numerical solution is shown to be in good quantitative agreement with estimates made from analytic models. Detailed examination of the solutions in the vicinity of the mode conversion location shows that the classic plane wave assumption fails to describe the true nature of the modes.

[a)]pbellan@caltech.edu

I. INTRODUCTION

Wave propagation in a magnetized plasma has been studied for a century and thousands of papers have been written on this subject. These waves have also been discussed in many books such as Stix[1], Swanson[2], and Bellan[3].

A wave of particular interest is the whistler wave which was first observed in a terrestrial context and has since been observed by spacecraft in Earth's magnetosphere and in the magnetospheres of other planets. Whistler waves have also been observed and studied extensively in laboratory plasmas. Magnetospheric whistler waves play an important role in pitch-angle scattering of energetic electrons trapped in Earth's Van Allen radiation belts causing some electrons to leak into the loss-cone of Earth's magnetic field and then impact Earth's upper atmosphere to form aurora.

Previous work on whistler waves will now be summarized. The first published report of whistler wave observation was by Barkhausen[4] in 1919 who stated that during the First World War unexpected audio frequency waves were detected from telephone lines at the front. These telephone lines were connected to high-gain amplifiers and an audible signal was heard that sounded like "shells flying". The signal was a descending audio tone lasting about a second. At first it was thought that these waves were related to a meteorological feature, but Barkhausen stated this was refuted because the telephone wires were underground. Barkhausen concluded that the cause of these waves was inexplicable and hoped that an understanding would be achieved in the future.

The cause of whistler waves remained unexplained until 1953 when Storey[5], using detailed observations of the geographical and temporal properties of whistler waves, concluded that whistler waves were excited by terrestrial lightning bolts. Storey postulated that these waves reflect back and forth between magnetically conjugate locations in the northern and southern hemispheres. This postulation was remarkable for two reasons: First, the required plasma density greatly exceeded the value assumed by then-existing models for the space regions through which the waves would have to propagate. Second, even if the waves could travel along the proposed path, they would be expected to have such a large geometrical divergence that their amplitude would become negligible after traveling from one hemisphere to the other. Storey boldly predicted that the plasma density along the wave trajectory must be much higher than what was then assumed; this prediction was later confirmed by spacecraft measurements in what is now known as the plasmasphere. However, the lack of geometric divergence could only be explained if the whistler waves were somehow channeled along a magnetic field line when bouncing between hemispheres. Such

channeling implies existence of some kind of waveguide or 'duct' connecting the two hemispheres so that the wave is confined to this duct.

Early models of whistler wave ducting invoked wave ray descriptions. An important example is that by Gendrin[6] who used a ray description to show that, for certain parameters, the wave group velocity would align exactly along the background magnetic field so that a wave would bounce between hemispheres along the background magnetic field with no power flow perpendicular to the magnetic field. However, it was later realized[7–11] that a ray description is inappropriate because the ray description ('geometric optics') is a form of the WKB approximation and so is based on the assumption that wave properties change very gradually over a wavelength. The whistler dispersion relation becomes quite complicated at the location where the reflection from the 'duct walls' is supposed to occur, and this complexity invalidates a ray description. In particular, as noted by Karpman[12], the assumption that wave properties change gradually (WKB approximation) is violated at the duct walls. Thus, a so-called 'full-wave' description must be used where the actual field differential equations are solved directly without invoking a geometric-optics WKB approximation.

Stenzel observed that high power whistler waves could effectively dig their own ducts[13]; the nonlinear ponderomotive force associated with the wave was seen to create a density depletion along the magnetic field in a laboratory plasma. The whistler wave maintained a constant amplitude as it propagated away from the excitation source, a behavior that contrasts with the non-duct situation where it was observed that wave amplitude decreased with distance from the source because of geometric divergence. Kostrov et al.[14] showed that ducts can also appear due to plasma heating because of a redistribution of the plasma away from the heated region by thermally driven diffusion.

Plasma wave models typically use a Cartesian geometry $\{x, y, z\}$ where z denotes the direction of the background magnetic field, x denotes the direction of density or background magnetic field inhomogeneity, and y is an ignorable coordinate so no quantity depends on y. However, instead of using Cartesian geometry, Kostrov et al.[14], Pasmanik and Trakhtengerts[8], Bakharev et al.[15], Kudrin et al.[16], and Nassiri-Mofakham[17] used a cylindrical coordinate system $\{r, \phi, z\}$ where z again denotes the background magnetic field, but now r denotes the distance from the magnetic field line that is the axis of a duct. Here ϕ is ignorable on the basis that the duct is azimuthally symmetric. Zudin et al.[18] considered both Cartesian and cylindrical models of whistler propagation.

Cho[19] and Nejad and Streltsov[11] independently concluded that whistler ducting involves a si-

multaneous mode conversion of a fast wave into a slow wave and mode conversion of a slow wave into a fast wave. Linear mode conversion (see Chapter 13 of Stix[1]) is a wave process that occurs when a wave equation is fourth order and, for a given frequency and parallel wavenumber, two distinct modes exist having perpendicular wavevectors that are normally distinct from each other, but become identical at a certain critical location. The two modes are labelled as 'fast' and 'slow' referring to the wave phase velocity in the direction perpendicular to the background magnetic field. For example, a fast mode propagating from left to right in a certain geometry and approaching the critical location converts into a slow mode that then propagates from right to left; there is also an associated 'tunneling' field to the right of the mode conversion location. Similarly, an approaching slow mode propagating from left to right converts into a fast mode that then propagates in the reverse direction and again there is an associated 'tunneling' field to the right of the mode conversion location. Thus, mode conversion is akin to reflection except that the reflected wave has been converted from fast to slow or vice versa. This simultaneous fast to slow and slow to fast mode conversion thus effectively acts as a mirror at the inside wall of the duct and so confines the whistler wave to the duct interior. Cho used cylindrical geometry, considered laboratory plasmas where the waves are called helicons and characterized the waves in terms of Hankel functions. Nejad and Streltsov used Cartesian geometry, compared their numerically calculated results to spacecraft measurements, called the process 'mode switching' and showed via numerical solutions that the mode switching would occur at a density dip. They also reported more complicated processes[20] that would occur where there is a local abrupt change in the magnetic field or in the density and called these locations density or magnetic shelves. These other more complicated processes appeared to be leaky because they appeared to have waves escaping the 'shelf'.

Maggs et al.[21] created a duct in a laboratory plasma and saw evidence of the co-existence of fast and slow waves. Streltsov et al.[10] have modeled a laboratory ducting experiment. The possibility of whistler waves in the solar corona has been considered[22] as well as in the solar wind[23].

Verkhoglyadova et al[24] have shown that the magnetic field of an oblique whistler wave is circularly polarized and that in certain limits becomes a Gendrin mode. Loi et al[25] directly imaged actual ducts using the Murchison Widefield Array radio telescope. Huba et al[26] have proposed that ducts can be produced by atmospheric gravity waves and provided models showing a plasmasphere with a corrugated density. Harid et al.[27] used a ray tracing code to model detailed spacecraft measurements but acknowledged that ray tracing fails at the location where the wave reflects. Gu et al.[28] have made a statistical study of duct size using 7 years of Van Allen spacecraft data.

Lewis and Bellan[29] showed that the requirement that physically measurable variables be non-singular coupled with cylindrical symmetry provided constraints on allowed dependence of variables; these regularity constraints provide insights into the nature of solutions to equations before solving these equations.

This paper begins by summarizing the uniform plasma model (i.e., dispersion relation) of whistler wave propagation and its WKB-like extension to a non-uniform plasma. The paper then derives an accurate pair of coupled differential equations that provide a 'full-wave' description of whistler wave propagation in a cylindrical duct and relates the solution of these equations to the simpler, but inaccurate, uniform plasma dispersion relation and WKB solutions. Although incorrect for a non-uniform plasma in the critical situation of interest, the uniform plasma dispersion relation and the related WKB solution serve as useful intuitive guides for interpretation of the accurate, but much more complicated, full-wave description.

The paper is organized as follows: Section II summarizes the uniform plasma whistler wave model expressed as a dispersion relation predicting two wave modes (fast and slow) that exist simultaneously while having the same parallel wavelength but different perpendicular wavelengths. The discussion further shows that there is a critical density, called the Gendrin density, at which the fast and slow waves have the same perpendicular wavelength and that for this density, the wave has the peculiar property of having zero energy flux perpendicular to the magnetic field. Section III derives the two coupled differential equations which constitute the full-wave description in the cylindrical geometry appropriate for a pipe-like duct. Section IV considers the Poynting vector in the context of the full wave equations and shows that the nature of these equations implies that there is zero energy flux perpendicular to the magnetic field at all radii in a non-uniform plasma; this result is a much stronger statement than the Gendrin density property of the uniform plasma analysis. Section V shows that the full-wave description can be reduced to the uniform plasma description and Section VI shows that this reduction retrieves the well-known limits of the uniform plasma description for propagation exactly parallel to or exactly perpendicular to the magnetic field (right and left hand circularly polarized for pure parallel propagation, ordinary and extraordinary modes for pure perpendicular propagation). Section VIII shows that in a radially non-uniform plasma, the parallel refractive index is determined by the location where the fast and slow modes coalesce. Section VIII points out physically important differences between cylindrical geometry and Cartesian geometry. Section IX prescribes a reference azimuthally symmetric case where an inner uniform-density plasma is connected to an outer higher-density region by a non-uniform

density region. Whistler waves in this situation are examined by pushing the uniform plasma description up to and, what is later shown, beyond its limits; while the results are later shown to be inexact, they nevertheless provide useful initial insights and benchmarks. Section X presents the numerical solution of the full-wave equations and relates this exact solution to the inexact but intuitive analytic results of Section IX. Section X then describes in detail the numerical method and its complexities, shows that the results indeed solve the equations and addresses an interesting issue related to the failure of the geometric-optics WKB approximation at the location where the fast and slow modes coalesce. The resolution of this issue reveals a new and unexpected type of solution that exists in the vicinity of the mode coalescence location. Section XI presents three cases differing from the reference case so as to demonstrate how the full-wave solution depends on the location of the mode coalescence and on frequency. Section XII presents a conclusion that summarizes the main results.

II. SUMMARY OF DISPERSION RELATION METHODS

SI units will be used. The plasma is assumed to have a background magnetic field $\mathbf{B} = B_0\hat{z}$ and the wave amplitude is assumed to be so small that a linear description can be used. The wave fields obey Maxwell's equations and the charged particles obey the Lorentz force equation. The wave is assumed to have a parallel phase velocity greatly exceeding both electron and ion thermal velocities and the particle temperatures are assumed to be sufficiently low that finite Larmor orbit effects can be neglected so the wave can be considered to be a cold plasma wave. The cold plasma wave dispersion relations are obtained from the determinant of a 3×3 matrix that multiplies the vector electric field and these dispersion relations are conveniently categorized by the CMA (Clemmo-Mullaly-Allis) diagram[1]. The CMA diagram is based on Cartesian geometry $\{x,y,z\}$ and all wave field components are assumed (e.g., see page 4 of Stix[1]) to have a plane-wave dependence given by

$$\mathbf{E}(x,y,z,t),\ \mathbf{B}(x,y,z,t) \sim e^{ik_x x + ik_z z - i\omega t} \tag{1}$$

where ω is assumed to be real and positive. Equation 1 is called the 'plane wave assumption' and is only strictly true if the plasma is spatially uniform. If the plasma is non-uniform in some direction, which in this paper will be the x direction, then in certain situations, the plane wave assumption may be generalized by the WKB approximation which allows for a spatially dependent $k_x(x)$, but

this generalization requires that $k_x(x)$ change very gradually in a wavelength and this requirement is violated in the situation of most interest here. Despite this breakdown, it is useful to consider the predictions of the plane wave and WKB solutions in a non-uniform plasma as these predictions provide useful insight. Thus, plane wave and WKB solutions will be discussed with appropriate warnings regarding where and how these solutions fail.

Plane waves are deemed to be "propagating" if $k^2 = k_x^2 + k_z^2 > 0$. The CMA diagram shows that thirteen qualitatively different regions exist for plane waves in a two-dimensional parameter space[1] and in each CMA region there can be zero, one, or two propagating wave modes. The $e^{ik_x x + ik_z z - i\omega t}$ dependence is invoked in Maxwell's equations and in the particle equations of motion to obtain a dispersion relation $\omega = \omega(\mathbf{k})$ that characterizes the mode properties. The refractive index $\mathbf{N} = c\mathbf{k}/\omega$, a parameter comparing waves in plasma to waves in vacuum, provides a convenient way to classify propagating modes as being fast (small N) or slow (large N). The whistler wave exists in the CMA region where $\omega_{pe}, \omega_{ce} \gg \omega \gg \omega_{ci}, \omega_{pi}$. An unexpected and important result of the analysis presented here is a demonstration that the seemingly innocuous assumption prescribed by Eq.1 fails in the vicinity of the mode conversion location; this demonstration will be given in Sec.X D.

The whistler dispersion relation is a simpler form of the rather complicated dispersion relations produced by the CMA analysis. This involves algebraic manipulations that produce the general Appleton-Hartree dispersion relation[1] and then further simplification based on assumptions regarding a parameter θ defined by $N_z/N = \cos\theta$. This simpler form is

$$N^2 = 1 + \frac{\omega_{pe}^2}{\omega\left(|\omega_{ce}|N_z/N - \omega\right)}; \tag{2}$$

the absolute value bars are used because $\omega_{ce} = q_e B/m_e$ is negative. As conventionally defined, here $\omega_{pe}^2 = nq_e^2/\varepsilon_0 m_e$ is the square of the electron plasma frequency while n is the electron density. θ is conventionally interpreted as a geometric angle between $\mathbf{N}$ and $\hat{z}$ so that $\cos\theta \leq 1$. However, when discussing mode conversion, this interpretation turns out to be inadequate because it omits the physically realistic and important situation where θ is complex so there is no geometric interpretation. The whistler regime typically has ω_{pe}^2 sufficiently large that the "1" on the right hand side (displacement current) can be discarded. We will alternate between using Eq.2 with displacement current dropped and using the full cold plasma dielectric tensor because useful insights are obtained from both these approaches and from comparing them.

On discarding displacement current, Eq.2 reduces to

$$N^2 = \frac{\omega_{pe}^2}{\omega\left(|\omega_{ce}|N_z/N - \omega\right)}; \tag{3}$$

discarding displacement current means that the upper hybrid resonance can no longer be described. It is now more convenient to use $\mathbf{k} = \omega\mathbf{N}/c$ instead of $\mathbf{N}$ so Eq.3 becomes

$$k^2 = \frac{\omega\omega_{pe}^2/c^2}{|\omega_{ce}|k_z/k - \omega}. \tag{4}$$

Equation 4 can be arranged as

$$k_x^2 + k_z^2 - \frac{|\omega_{ce}|}{\omega}k_z\sqrt{k_x^2 + k_z^2} + \frac{\omega_{pe^2}}{c^2} = 0. \tag{5}$$

Streltsov and colleagues have shown that Eq.5 can be solved for k_x^2 to give two modes, denoted slow (subscript 's') and fast (subscript 'f'),

$$k_{xs}^2 = k_z^2\left[\left(\frac{\omega_{ce}}{2\omega}\right)^2\left(1 + \sqrt{1 - \frac{n}{n_G}}\right)^2 - 1\right] \tag{6}$$

$$k_{xf}^2 = k_z^2\left[\left(\frac{\omega_{ce}}{2\omega}\right)^2\left(1 - \sqrt{1 - \frac{n}{n_G}}\right)^2 - 1\right] \tag{7}$$

where n_G, called the Gendrin density, is given by

$$n_G = \frac{1}{4}\frac{\varepsilon_0 m_e \omega_{ce}^2}{e^2}N_z^2 \tag{8}$$

so

$$\frac{\omega_{pe}^2}{\omega_{ce}^2} = \frac{N_z^2}{4} \text{ at } n = n_G. \tag{9}$$

If the plasma is spatially uniform and has a density $n = n_G$ the fast and slow modes become indistinguishable. On the other hand, if the plasma is spatially non-uniform so that there is a specific x at which $n(x) = n_G$, then the situation develops an inherent paradox. The paradox results because the location where the two plane wave modes become indistinguishable is precisely the location where the plane wave model (and its WKB generalization) break down. Resolving this paradox is one of the main results of this paper. The plane wave approximation and its WKB extension will be used to the extent that they provide useful intuition and the cause of the breakdown will be examined. The nature of the breakdown will be compared to the correct full-wave solution. Thus, the prediction that the plane wave solutions become indistinguishable in a non-uniform

plasma at $n(x) = n_G$ is formally meaningless because the plane wave assumption and the resulting concept of dispersion relations are not permissible at $n(x) = n_G$. Despite this, it is nevertheless helpful to intuition to be aware of the predictions of the plane wave/WKB model and its associated dispersion relations; these predictions, while not correct, serve as a guide/benchmark/insight for understanding what actually happens. Thus, the uniform plasma prediction that the fast and slow modes become indistinguishable at $n = n_G$ provides the insight that in a non-uniform plasma the fast and slow modes strongly interact at $n(x) = n_G$.

The dispersion relation can be expressed in terms of 'natural' parameters by defining

$$\bar{\omega} = \omega/|\omega_{ce}| \tag{10}$$

$$d_e = c/\omega_{pe} \tag{11}$$

$$\bar{k}_z = k_z d_e \tag{12}$$

$$\bar{k}_x = k_x d_e \tag{13}$$

where d_e is the electron skin depth. Using these definitions, Eq.5 reduces to

$$\bar{k}^2 + 1 = \bar{k}\bar{k}_z/\bar{\omega}. \tag{14}$$

In the $\bar{k}_x \to 0$ limit, $\bar{k}_z \to \bar{k}$ and the dispersion relation reduces to

$$\bar{k} = \sqrt{\frac{\bar{\omega}}{1-\bar{\omega}}}. \tag{15}$$

This can be expressed in terms of the axial wavelength $\lambda_z = 2\pi/k_z$, the quantity typically measured in experiments, as

$$\lambda_z = \frac{c}{f_{pe}}\sqrt{\frac{f_{ce}}{f} - 1} \tag{16}$$

so if for example $f/f_{ce} = 1/2$, then $\lambda_z = c/f_{pe}$; here $f = \omega/2\pi$ and $f_{ce} = |\omega_{ce}|/2\pi$. Equivalently, Eq.14 can be expressed as

$$\frac{f}{f_{ce}} = \frac{\bar{k}^2}{\bar{k}^2 + 1} \tag{17}$$

a relation verified experimentally in Fig.6 of Stenzel[30] where $d_e = c/\omega_{pe} = 1.07$ cm on using $\omega_{pe}/\omega_{ce} = 19$ and $|\omega_{ce}|/2\pi = 235$ MHz. This shows that for $0.2 < f/f_{ce} < 0.6$, a typical range for whistler experiments and observations, the axial wavelength ranges from half to one and a half times c/f_{pe}. For purposes of rough estimation, the λ_z of a whistler wave in the range $0.2 < f/f_{ce} < 0.6$ can be considered to scale approximately inversely with frequency with the condition

that $\lambda_z = c/f_{pe}$ when $f/f_{ce} = 1/2$. These approximations are true only if the radial wavelength is much larger than λ_z and since the radial wavelength is of the order of the device radius l_{device}, this requires l_{device} to be much larger than $2\pi d_e$, a condition that places a lower bound on the electron density. Thus, to satisfy these conditions it is necessary to have $l_{device} \gg 2\pi c/\omega_{pe}$ which corresponds to requiring $n \gg 4\pi^2 m_e/(\mu_0 q_e^2 l_{device}^2)$. For example, if the device radius is $l_{device} =$ 0.5 m, then the electron density should satisfy $n \gg 4\times 10^{15}$ m^{-3}. In lab experiments reporting whistler wave observations, this condition is typically satisfied by a margin of about 10^2.

Another point of view is obtained by squaring and expanding Eq.5 which becomes the quadratic equation in $\bar{k}_x^2$,

$$\bar{k}_x^4 + \left(2\bar{k}_z^2 - \frac{\bar{k}_z^2}{\bar{\omega}^2} + 2\right)\bar{k}_x^2 + \left(\bar{k}_z^4 - \bar{k}_z^2\left(\frac{\bar{k}_z^2}{\bar{\omega}^2} - 2\right) + 1\right) = 0. \tag{18}$$

Solving for $\bar{k}_x^2$ gives the two roots

$$\bar{k}_x^2 = \bar{k}_z^2\left(-1 + \frac{1}{2\bar{\omega}^2} - \frac{1}{\bar{k}_z^2} \pm \frac{1}{2\bar{\omega}^2}\sqrt{1 - \frac{4\bar{\omega}^2}{\bar{k}_z^2}}\right). \tag{19}$$

These roots merge when $\bar{k}_z^2 = 4\bar{\omega}^2$ which corresponds to the Gendrin relation, Eq.9. The value of the merged root is

$$\left(\bar{k}_x^2\right)_{merged} = \bar{k}_z^2\left(\frac{1}{4\bar{\omega}^2} - 1\right). \tag{20}$$

In order for this merged root to be positive and hence associated with propagating modes just before merging, it is necessary to have $\bar{\omega} < 1/2$.

Equation 20 indicates that $\left(\bar{k}_x^2\right)_{merged} = \bar{k}_z^2$ when $\bar{\omega} = 1/\sqrt{8} = 0.353$ in which case wave phase fronts would propagate at a 45 degree angle relative to the magnetic field. This 45 degree angle was observed by Stenzel and Urrutia[31] in a laboratory experiment having $B = 5\times 10^{-4}$ T so $f_{ce} = 1.4\times 10^7$ Hz and the wave frequency was $f = 5$ MHz so $\bar{\omega} = f/f_{ce} = 0.357 \approx 1/\sqrt{8}$. This experiment had an axial wavelength $\lambda_z = 0.14$ m so $N_z = c/(f\lambda_z) = 429$. Equation 8 predicts that the Gendrin density will then be

$$n_G = \frac{1}{4}\frac{\varepsilon_0 B^2}{m_e}N_z^2 = 1.1\times 10^{17}\mathrm{m}^{-3} \tag{21}$$

which is in good agreement with the reported density of 10^{17} m^{-3}.

Another constraint, to be justified below, is that for the fast mode to exist, it is necessary to have $N_z^2 < \frac{\omega_{pe}^2/\omega_{ce}^2}{\bar{\omega}(1-\bar{\omega})}$ in the limit that displacement current can be neglected. The conditions for having

fast and slow modes exist and then merge at some location are summarized as

$$\bar{\omega} \; < \; \frac{1}{2} \tag{22}$$

$$\frac{4\omega_{pe}^2}{\omega_{ce}^2} \; < \; N_z^2 < \frac{\omega_{pe}^2/\omega_{ce}^2}{\bar{\omega}\,(1-\bar{\omega})}. \tag{23}$$

When Eqs.22 and 23 are satisfied, the fast and slow modes are distinct and both $N_{\perp s}^2$ and $N_{\perp f}^2$ are pure real. The fast mode has an electromagnetic character and is right hand circularly polarized whereas the slow mode has an electrostatic character.

As shown by Gendrin[6], Helliwell[32], and Verhoglyadova et al.[24], there is a special situation, called the 'Gendrin mode' where the z components of the wave group and phase velocities are equal. This equality has been experimentally validated (see Fig. 8c of Urratia and Stenzel[33]).

To derive the Gendrin mode, Eq.4 is re-arranged as

$$\omega = \frac{c^2}{\omega_{pe}^2}(|\omega_{ce}|k_z k - \omega k^2). \tag{24}$$

By taking the derivative of Eq.24 with respect to k_x, the x component of the group velocity is seen to be

$$\frac{\partial \omega}{\partial k_x} = \frac{c^2}{\omega_{pe}^2}\left(|\omega_{ce}|k_z - 2\omega k\right)\frac{\partial k}{\partial k_x}. \tag{25}$$

In the situation where

$$k = \frac{|\omega_{ce}|k_z}{2\omega} \tag{26}$$

it is seen that $\partial\omega/\partial k_x = 0$ so the group velocity is only in the z direction.

Using Eq.26 to substitute for k in Eq.24 gives

$$\omega = \frac{c^2}{\omega_{pe}^2}\frac{|\omega_{ce}|^2 k_z^2}{4\omega} \tag{27}$$

which upon rearrangement shows that the z direction phase velocity is

$$\frac{\omega}{k_z} = \frac{c\,|\omega_{ce}|}{2\omega_{pe}}. \tag{28}$$

This can be expressed as

$$\omega = \frac{c\,|\omega_{ce}|}{2\omega_{pe}}k_z \tag{29}$$

which implies

$$\frac{\partial \omega}{\partial k_z} = \frac{c\,|\omega_{ce}|}{2\omega_{pe}}. \tag{30}$$

Thus, the group velocity in the z direction equals the phase velocity in z the direction.

Equation 26 can be written as

$$\frac{\omega}{|\omega_{ce}|} = \frac{1}{2}\frac{k_z}{k} \leq \frac{1}{2} \tag{31}$$

which constrains ω for the Gendrin mode.

This discussion of group and phase velocities is only appropriate for a uniform plasma. In a plasma that is non-uniform in x but uniform in z a full-wave description must be used to analyze wave behavior. This is because the group velocity is equivalent to the geometric optics ray concept and so depends on the WKB assumption $k_x^{-1}dk_x/dx \ll k_x$ which fails at the mode conversion location because at this location $dk_x/dx \to \infty$. For example, if the density n depends on x, then taking the derivative of Eq.6 or of Eq.7 with respect to x shows that $dk_x/dx \to \infty$ at the location where $n(x) \to n_G$. Although the concept of group velocity in the x direction, i.e., $v_{g,x} = \partial\omega/\partial k_x$ fails at the mode conversion location, the concept of group velocity in the z direction,i.e., $v_{g,z} = \partial\omega/\partial k_z$ remains valid at all positions.

This breakdown of the group velocity concept at the mode conversion location can also be seen from consideration of the standard derivation of group velocity, as exemplified by Jackson[34] where the derivation has a logic progressing from Eq.7.6 (p.296, equivalent to Eq.1 here), to Eq. 7.80 (superposition of Eq.1 solutions in a Fourier integral) to Eq.7.84 (coherent phase mixing on the group velocity trajectory). It will be shown in Section X D of this paper that the Eq.1 assumption is inadequate at the mode conversion location so the logical progression summarized above fails because of the failure of the first assumption in this logical progression, namely the assumption that propagation is completely prescribed by Eq.1.

III. FUNDAMENTAL EQUATIONS INSTEAD OF DISPERSION RELATIONS

Instead of assuming a uniform plasma which enables use of the dispersion relations summarized in the previous section, we now use the original wave partial differential equations. However, we will also refer back to the dispersion relation results as they provide useful benchmarks and insights regarding the more fundamental differential equation analysis. Cold plasma waves are traditionally described using the wave electric field vector **E** as the fundamental parameter. The wave dispersion relation is then derived from the determinant of a 3×3 matrix that multiplies **E** and results from combining Ampere's law, Faraday's law and the Lorentz force equation. Knowing **E**, the wave magnetic field **B** can then be determined from Faraday's law. In Bellan[35] it was shown

that simpler and more transparent forms of dispersion relations can be obtained by optimal choice of the fundamental parameter. Following this approach, we will use the wave magnetic field **B** as the fundamental parameter. This provides a significant advantage because the zero-divergence property of the magnetic field means that the wave magnetic field can be characterized by just two scalar parameters whereas the wave electric field requires three quantities. Furthermore, we assume that both the wave and the environment are cylindrically axisymmetric so the coordinate system is cylindrical with coordinates $\{r,\phi,z\}$ where the z axis passes through the source and the wave has no ϕ dependence. This axisymmetric wave assumption precludes consideration of waves having $\exp(im\phi)$ spatial dependence where m is a non-zero integer; effectively it is assumed that the wave has $m=0$ azimuthal dependence. The assumption of axisymmetry for the environment is the natural coordinate system of a pipe or tube with axis on a magnetic field line linking a location in Earth's northern hemisphere to a magnetically conjugate location in Earth's southern hemisphere. The virtue of $\{r,\phi,z\}$ cylindrical geometry compared to $\{x,y,z\}$ Cartesian geometry is that ϕ has the finite domain from 0 to 2π which relates to a real physical geometry whereas y has an infinite domain, namely $-\infty < y < \infty$ which does not correspond to a real physical geometry.

We now derive two coupled equations involving the wave magnetic field. The equations presented here are mathematically equivalent to the conventional electric-field cold plasma plane-wave description but incorporate certain insights and practical advantages.

As before, we assume a time dependence $e^{-i\omega t}$ so Faraday's and Ampere's laws are

$$\nabla\times\mathbf{E} \;=\; i\omega\mathbf{B} \tag{32}$$

$$\nabla\times\mathbf{B} \;=\; -i\frac{\omega}{c^2}\mathbf{K}\cdot\mathbf{E} \tag{33}$$

where the plasma dielectric tensor **K** is such that

$$\mathbf{K}\cdot\mathbf{E} = S\mathbf{E}_\perp + iD\hat{z}\times\mathbf{E}_\perp + PE_z\hat{z}; \tag{34}$$

here $\perp$ means in the direction perpendicular to $\hat{z}$. The cold plasma dielectric tensor elements are[1]

$$S = 1-\sum_{\sigma=i,e}\frac{\omega_{p\sigma}^2}{\omega^2-\omega_{c\sigma}^2},\; D=\sum_{\sigma=i,e}\frac{\omega_{c\sigma}}{\omega}\frac{\omega_{p\sigma}^2}{\omega^2-\omega_{c\sigma}^2},\; P=1-\sum_{\sigma=i,e}\frac{\omega_{p\sigma}^2}{\omega^2}. \tag{35}$$

We have used Stix's notation for the dielectric tensor elements because of convenience of the mnemonics: $S=$ sum, $D=$ difference, $P=$ parallel with associated quantities $R=$right and $L=$ left

so $S=(R+L)/2$ (sum) and $D=(R-L)/2$ (difference). Thus,

$$R = S+D \tag{36}$$

$$L = S-D. \tag{37}$$

We define

$$\bar{\mathbf{r}} = \mathbf{r}\omega/c \tag{38}$$

and

$$\bar{\nabla} = \frac{c}{\omega}\nabla \tag{39}$$

so Eqs.32 and 33 become

$$\bar{\nabla}\times\mathbf{E} = ic\mathbf{B} \tag{40}$$

$$\bar{\nabla}\times c\mathbf{B} = -i\mathbf{K}\cdot\mathbf{E}. \tag{41}$$

Because the wave fields do not depend on ϕ, the wave magnetic field can be expressed in the general *two-parameter* form

$$c\mathbf{B} = \bar{\nabla}\psi\times\bar{\nabla}\phi + \chi\bar{\nabla}\phi \tag{42}$$

where ψ is proportional to the wave poloidal magnetic flux and χ is proportional to the wave poloidal magnetic current consisting of the sum of the wave plasma and displacement currents. Here $\bar{\nabla}\phi = \hat{\phi}/\bar{r}$, poloidal refers to vectors in the r,z plane, and toroidal refers to a vector in the ϕ direction. Equation 42 shows that $\mathbf{B}\cdot\bar{\nabla}\psi = 0$ indicating that poloidal magnetic field lines are contours of constant ψ. Equation 42 is the most general form for an axisymmetric magnetic field because it depends on two independent scalar functions and automatically satisfies $\bar{\nabla}\cdot\mathbf{B}=0$ since $\bar{\nabla}\cdot\left(\bar{\nabla}\psi\times\bar{\nabla}\phi\right)=0$ for arbitrary ψ and $\bar{\nabla}\cdot\left(\chi\bar{\nabla}\phi\right)=\chi\bar{\nabla}^2\phi=0$ for arbitrary $\chi(\bar{r},\bar{z})$. The condition $\bar{\nabla}\cdot\mathbf{B}=0$ implies that a magnetic field depends on only two scalar functions because once any two components of $\mathbf{B}$ are specified, the third component is determined from $\bar{\nabla}\cdot\mathbf{B}=0$. This situation is not true for the electric field because $\bar{\nabla}\cdot\mathbf{E}$ can be non-zero. $\psi(\bar{r},\bar{z})$ has the physical interpretation of being the magnetic flux (except for a constant coefficient) passing through a circle about the $\bar{z}$ axis having radius $\bar{r}$ and axial position $\bar{z}$. Similarly, $\chi(\bar{r},\bar{z})$ has the physical interpretation of being the current (plasma and displacement) passing through a similar circle, again except for a constant coefficient. Equivalently, χ can be interpreted as an expression of Ampere's law which states that $B_\phi \sim I/\bar{r}$ where I is the current passing through a circle of radius $\bar{r}$.

The wave magnetic field components are then

$$B_r = -\frac{1}{\bar{r}c}\frac{\partial \psi}{\partial \bar{z}} \tag{43}$$

$$B_\phi = \frac{\chi}{\bar{r}c} \tag{44}$$

$$B_z = \frac{1}{\bar{r}c}\frac{\partial \psi}{\partial \bar{r}}. \tag{45}$$

Taking the curl of Eq.42 gives

$$\bar{\nabla} \times c\mathbf{B} = -\bar{r}^2 \bar{\nabla} \cdot \left(\frac{1}{\bar{r}^2}\bar{\nabla}\psi\right)\bar{\nabla}\phi + \bar{\nabla}\chi \times \bar{\nabla}\phi \tag{46}$$

so Eqs. 40 and 41 can be expressed as

$$\bar{\nabla} \times \mathbf{E} = i\bar{\nabla} \times \left(\psi \bar{\nabla}\phi\right) + i\chi\bar{\nabla}\phi \tag{47}$$

$$-\bar{r}^2 \bar{\nabla} \cdot \left(\frac{1}{\bar{r}^2}\bar{\nabla}\psi\right)\bar{\nabla}\phi + \bar{\nabla}\chi \times \bar{\nabla}\phi = -iS\mathbf{E}_\perp + D\hat{z} \times \mathbf{E}_\perp - iPE_z\hat{z}. \tag{48}$$

Because the curl of a poloidal vector is toroidal and vice versa, decomposing Eq.47 into toroidal and poloidal components gives

$$\bar{\nabla} \times \mathbf{E}_{pol} = i\chi\bar{\nabla}\phi \tag{49}$$

$$\bar{\nabla} \times \mathbf{E}_{tor} = i\bar{\nabla} \times \left(\psi\bar{\nabla}\phi\right). \tag{50}$$

Integration of Eq.50 gives

$$\mathbf{E}_{tor} = i\psi\bar{\nabla}\phi \tag{51}$$

so

$$E_\phi = i\frac{\psi}{\bar{r}}. \tag{52}$$

Dotting Eq.49 with $\hat{\phi}$ gives

$$\frac{\partial E_r}{\partial \bar{z}} - \frac{\partial E_z}{\partial \bar{r}} = \frac{i\chi}{\bar{r}}. \tag{53}$$

Dotting Eq.48 with $\hat{r}, \hat{\phi}, \hat{z}$ successively gives

$$\frac{1}{\bar{r}}\frac{\partial \chi}{\partial \bar{z}} = iSE_r + DE_\phi \tag{54}$$

$$-\bar{r}\bar{\nabla} \cdot \left(\frac{1}{\bar{r}^2}\bar{\nabla}\psi\right) = -iSE_\phi + DE_r \tag{55}$$

$$\frac{i}{\bar{r}}\frac{\partial \chi}{\partial \bar{r}} = PE_z. \tag{56}$$

Substituting for E_ϕ in Eqs.54 and 55 and substituting for E_z in Eq.53 provides

$$-\frac{i}{\bar{r}}\frac{\partial \chi}{\partial \bar{z}} = SE_r + D\frac{\psi}{\bar{r}} \tag{57}$$

$$-\bar{r}\bar{\nabla}\cdot\left(\frac{1}{\bar{r}^2}\bar{\nabla}\psi\right) = S\frac{\psi}{\bar{r}} + DE_r. \tag{58}$$

$$\frac{\partial E_r}{\partial \bar{z}} - i\frac{\partial}{\partial \bar{r}}\left(\frac{1}{P\bar{r}}\frac{\partial \chi}{\partial \bar{r}}\right) = \frac{i\chi}{\bar{r}}. \tag{59}$$

Solving Eq.57 for E_r gives

$$E_r = -\frac{i}{S\bar{r}}\left(\frac{\partial \chi}{\partial \bar{z}} - iD\psi\right) \tag{60}$$

and substituting this into Eqs. 58 and 59 gives two coupled partial differential equations involving ψ and χ, namely

$$\bar{r}\frac{\partial}{\partial \bar{r}}\left(\frac{1}{\bar{r}}\frac{\partial \psi}{\partial \bar{r}}\right) + \frac{\partial^2 \psi}{\partial \bar{z}^2} + \frac{S^2 - D^2}{S}\psi = \frac{iD}{S}\frac{\partial \chi}{\partial \bar{z}} \tag{61}$$

$$\bar{r}\frac{\partial}{\partial \bar{r}}\left(\frac{1}{P\bar{r}}\frac{\partial \chi}{\partial \bar{r}}\right) + \frac{\partial}{\partial \bar{z}}\left(\frac{1}{S}\frac{\partial \chi}{\partial \bar{z}}\right) + \chi = i\frac{\partial}{\partial \bar{z}}\left(\frac{D}{S}\psi\right). \tag{62}$$

If we now assume that there is an $\exp(ik_z z) = \exp(iN_z\bar{z})$ dependence where $N_z = ck_z/\omega$ and $\bar{z} = z\omega/c$, Eqs.61 and 62 become

$$\bar{r}\frac{\partial}{\partial \bar{r}}\left(\frac{1}{\bar{r}}\frac{\partial \psi}{\partial \bar{r}}\right) + \left(\frac{S^2 - D^2}{S} - N_z^2\right)\psi = -N_z\frac{D}{S}\chi \tag{63}$$

$$\bar{r}\frac{\partial}{\partial \bar{r}}\left(\frac{1}{P\bar{r}}\frac{\partial \chi}{\partial \bar{r}}\right) + \left(1 - \frac{N_z^2}{S}\right)\chi = -N_z\frac{D}{S}\psi. \tag{64}$$

These two equations are equivalent to the determinant of the 3×3 matrix associated with the CMA diagram but have the advantages of: (i) involving only two quantities, namely ψ and χ, (ii) involve cylindrical geometry, (iii) allow for both density and background magnetic field radial gradients, and (iv) provide regularity constraints that are missing from a Cartesian geometry model.

By using Eq.52 to give $\psi = -irE_\phi$ and $\chi = \bar{r}cB_\phi$, Eqs.63 and 64 become identical to Eqs.18(a,b) in Kostrov et al.[14]. Kostrov solved the equations by assuming a Bessel function solution for an inner uniform density region and a Hankel function solution for an outer, but different, uniform density region and then used boundary conditions at the step interface to connect the inner and outer solutions. Kostrov et al. stated that there were no discernible differences between the step solution and a solution, not presented in Kostrov et al., having a more realistic smooth transition. Close examination of the solutions shown in Figs. 9 and 10 of Kostrov et al.

show discontinuities in the radial component of the wave electric field at the location where fast and slow modes merge; there are also discontinuities in the radial derivative of the axial electric field. As noted in the caption of Fig. 9 in Kostrov et al., these discontinuities are a consequence of the step approximation. The discontinuity in E_r implies a non-physical surface charge density at the merging location. The analysis presented here will not assume a step interface and so is not constrained by the simplifying step assumption inherent in Figs. 9 and 10 in Kostrov et al.

We note that instead of using Eqs.63 and 64 the cold plasma wave equations can be expressed as a pair of coupled equations in E_z and B_z but this alternative representation is far more complicated as seen from examination of Eqs.(81) and (82) in Bellan[36] and Eqs.(6) and (7) in Bakharev et al.[15].

An important and consequential feature of Eqs.63 and 64 is that all coefficients in these equations are real. This means that ψ and χ can be considered to both be pure real without loss of generality as real parts of ψ interact only with real parts of χ and imaginary parts of ψ interact only with imaginary parts of χ. Furthermore, it is impossible to have a solution where either one of ψ or χ is zero everywhere if $N_z D/S \neq 0$. Thus, the system is a true fourth order system where both ψ and χ must be finite. Equations 63 and 64 are notationally somewhat simpler than corresponding equations that describe the problem in terms of electric and magnetic fields (for example, compare Eqs.63 and 64 here to Eqs. (4) and (5) in Nassiri-Mofakham[17] or to Eqs.18(a,b) in Kostrov et al[14].

Using Eqs. 43, 45, 52, 56, and 60 the electric and magnetic field components are thus determined from ψ and χ as

$$\begin{aligned} E_r &= \frac{1}{S\bar{r}}\left(N_z\chi - D\psi\right) \\ E_\phi &= i\frac{\psi}{\bar{r}} \\ E_z &= \frac{i}{\bar{r}P}\frac{\partial\chi}{\partial\bar{r}} \\ B_r &= -\frac{iN_z}{\bar{r}c}\psi \\ B_\phi &= \frac{\chi}{\bar{r}c} \\ B_z &= \frac{1}{\bar{r}c}\frac{\partial\psi}{\partial\bar{r}}. \end{aligned} \tag{65}$$

Because E_r, E_ϕ, B_r, B_ϕ must all vanish at $\bar{r}=0$, it is necessary that both ψ and χ satisfy the regularity condition of being proportional to $\bar{r}^2$ at small $\bar{r}$. Contours of ψ show the projection of the magnetic field in the r,z plane while contours of χ show projections of the wave current vector (plasma and displacement) in the r,z plane.

IV. POYNTING VECTOR

The conclusion in the previous section that ψ and χ may be assumed to be real has important implications for the wave energy flux. For electromagnetic fields having time-dependence $\exp(-i\omega t)$ the time-averaged wave energy flux is given by the Poynting vector

$$\mathbf{\Pi} = \frac{1}{2\mu_0}\,\mathrm{Re}\,(\mathbf{E}\times\mathbf{B}^*)\,. \tag{66}$$

It should be noted that for a cold plasma wave as discussed here, the Poynting flux vector $\mathbf{\Pi}$ and the group velocity vector are collinear (see Eq.27 in Chapter 4 of Stix[1]). Since being real implies $\psi^* = \psi$ and $\chi^* = \chi$, on using Eq.65, the Poynting vector components are

$$\Pi_r = \frac{1}{2\bar{r}^2 c\mu_0}\,\mathrm{Re}\left(i\,\psi\frac{\partial\psi}{\partial\bar{r}} - \frac{i\chi}{P}\frac{\partial\chi}{\partial\bar{r}}\right) = 0 \tag{67}$$

$$\Pi_\phi = \frac{1}{2\bar{r}^2 c\mu_0}\left(\frac{D}{S}\psi\frac{\partial\psi}{\partial\bar{r}} - N_z\left(\frac{1}{P}\frac{\partial\chi}{\partial\bar{r}}\psi + \frac{\chi}{S}\frac{\partial\psi}{\partial\bar{r}}\right)\right) \tag{68}$$

$$\Pi_z = \frac{1}{2\bar{r}^2 c\mu_0}\left(-\frac{D}{S}\psi\chi + N_z\left(\psi^2 + \frac{\chi^2}{S}\right)\right). \tag{69}$$

Both Π_ϕ and Π_z are finite and depend on the sign of N_z so the wave energy flux follows a helix about the z axis. However, Eq. 67 shows that $\Pi_r = 0$ which means that the radial component of the group velocity is zero at all radii. This is a much stronger statement than Gendrin's observation that the group velocity vanishes when the fast and slow mode coalesce. If waves are confined to a duct, then it would be necessary to have $\Pi_r = 0$ everywhere. Equation 67 thus indicates that a ducting solution is possible for solutions to Eqs. 63 and 64 where χ and ψ are both real and obey physically allowable boundary conditions, namely regularity at $\bar{r} = 0$ and vanishing at $\bar{r} = \infty$. It was mentioned earlier that the concept of radial group velocity and the geometric-optics WKB approximation fail at the Gendrin density (location where fast and slow modes coalesce). However, this failure is not an issue for Eq.66 and in particular for Eq.67 which are always valid and so can be considered to be more fundamental.

V. UNIFORM PLASMA SOLUTIONS

Before addressing the ducting problem, we consider the simpler situation where S, P, and D are spatially uniform. The solutions of Eqs.63 and 64 are then of the form $\psi, \chi \sim \bar{r}J_1(N_r\bar{r})$ where J_1 is a Bessel's equation of order 1 and N_r is determined by a dispersion relation. Although $\bar{r}Y_1(N_r\bar{r})$ is

also a mathematically valid solution of Eqs.63 and 64, this solution is discarded because at small $\bar{r}$, $Y_1(N_r\bar{r}) \sim 1/\bar{r}$ which would predict the non-physical behavior of $B_r \sim 1/\bar{r}$ near $\bar{r} = 0$. Similarly, Hankel function solutions are not allowed as these involve linear combinations of J_1 and Y_1. Since a Bessel function of order 1 satisfies

$$\frac{d^2J_1}{ds^2} + \frac{1}{s}\frac{dJ_1}{ds} - \frac{1}{s^2}J_1 = -J_1 \tag{70}$$

evaluation of ψ and χ using Eq.70 shows that

$$\begin{aligned} \bar{r}\frac{\partial}{\partial\bar{r}}\left(\frac{1}{\bar{r}}\frac{\partial\psi}{\partial\bar{r}}\right) &= -N_r^2\psi, \\ \bar{r}\frac{\partial}{\partial\bar{r}}\left(\frac{1}{\bar{r}}\frac{\partial\chi}{\partial\bar{r}}\right) &= -N_r^2\chi. \end{aligned} \tag{71}$$

Using Eq.71 and defining $\bar{S} = S - N_z^2$, Eqs.63 and 64 reduce to

$$\left(-SN_r^2 + S\bar{S} - D^2\right)\psi = -N_z D\chi \tag{72}$$

$$\left(-SN_r^2 + \bar{S}P\right)\chi = -N_z PD\psi. \tag{73}$$

Setting the determinant of these coupled equations to zero gives

$$SN_r^4 - \left(\bar{S}(S+P) - D^2\right)N_r^2 + P\left(\bar{S}^2 - D^2\right) = 0 \tag{74}$$

a dispersion relation for N_r^2 which corresponds to the Cartesian plane wave dispersion in Puri and Tutter[37].

VI. REVERSION TO KNOWN LIMITS

Equations 63 and 64 revert to known limits for pure parallel and pure perpendicular propagation. If there is no dependence on $\bar{r}$ so $\partial/\partial\bar{r} = 0$, these equations reduce to

$$\left(\frac{S^2 - D^2}{S} - N_z^2\right)\psi = -N_z\frac{D}{S}\chi \tag{75}$$

$$\left(1 - \frac{N_z^2}{S}\right)\chi = -N_z\frac{D}{S}\psi. \tag{76}$$

Substituting for χ from Eq.76 in Eq.75 gives

$$\left(S - N_z^2\right)^2 = D^2 \tag{77}$$

so

$$S - N_z^2 = \pm D \tag{78}$$

implying the well-known result for pure parallel propagation

$$N_z^2 = R, L. \tag{79}$$

If N_z is assumed zero, then upon use of Eq.71, Eqs. 63 and 64 become

$$-N_r^2 \psi + \left(\frac{S^2 - D^2}{S} \right) \psi = 0 \tag{80}$$

$$-\frac{N_r^2}{P} \chi + \chi = 0. \tag{81}$$

Thus if ψ is finite and χ is zero, the dispersion relation is

$$N_r^2 = \frac{S^2 - D^2}{S} = \frac{RL}{S} \tag{82}$$

which is the 'extra-ordinary' dispersion while if χ is finite and ψ is zero, the dispersion relation is

$$N_r^2 = P \tag{83}$$

which is the 'ordinary' dispersion. Equation 65 gives the polarizations of the electric and magnetic fields of these modes.

VII. WHAT DETERMINES N_z

The experiments and magnetosphere are presumed to be infinitely long in the z direction so there are no direct boundary conditions to determine N_z. However, the dimensions are presumed to be finite in the r direction and so boundary conditions associated with r determine N_r or radial behavior. The ducted and non-ducted situations differ with regards to radial boundary conditions. In a plasma experiment where the plasma is radially uniform and the radius of the vacuum chamber is much larger than the electron skin depth, the radial wavelength is of the order of the chamber radius, i.e., $\partial/\partial \bar{r}$ is near zero and the dispersion relation is given by Eq.79. Because $L < 0$, the only propagating mode is $N_z \simeq R$, which corresponds to Eqs.15-17 and gives λ_z to be of the order of c/f_{pe}.

However, if there is a duct, then N_z is determined by Eq.8. This is because the ducting depends on there being a coalescence of the fast and slow modes which, as shown in Eqs. 6 and 7, occurs at the location where $n = n_G$. Because Eq.8 shows that n_G is proportional to N_z^2, this means that N_z^2 is determined by the location where the fast and slow modes coalesce, i.e., where $n = n_G$.

VIII. IMPLICATION OF CYLINDRICAL GEOMETRY COMPARED TO CARTESIAN GEOMETRY

The N_r refractive index component in cylindrical geometry corresponds to an N_x refractive index in Cartesian geometry. In Cartesian geometry it would be possible to have an isolated $e^{iN_x\bar{x}}$ solution which would correspond to having a wave propagating in the positive $\bar{x}$ direction. The corresponding cylindrical situation would be a wave propagating in the positive $\bar{r}$ direction and such a wave would involve a Hankel function $\bar{r}H_1^{(1)}(N_r\bar{r})$. However, since $H_1^{(1)}(N_r\bar{r}) = J_1(N_r\bar{r}) + iY_1(N_r\bar{r})$ and since $Y_1(N_r\bar{r})$ is forbidden because it diverges at $\bar{r}=0$, the only possibility is to have a function of the form $\bar{r}\left(H_1^{(1)}(N_r\bar{r}) + H_1^{(2)}(N_r\bar{r})\right) \sim \bar{r}J_1(N_r\bar{r})$. Thus, there must always be equal amounts of inward and outward waves, or equivalently, the requirement that field components are finite at $\bar{r}=0$ implies that there must be a standing wave in the radial direction. This conclusion is consistent with Eq.67 which indicates that there is no radial Poynting flux and with the condition that both ψ and χ are real.

IX. WHISTLER REGIME AND RELATION BETWEEN EQS.74 AND 18

Because we are interested in whistler wave ducting, we restrict consideration to the whistler regime where ion motion can be neglected. A set of relevant parameters and relationships will be established in this section, and for purposes of later comparison with a numerical calculation, quantitative values will be assigned, and then used to calculate intermediate quantities that can then be compared with the numerical calculation. To make it convenient to refer to results derived across sections when comparing the numerical solution to analytic predictions, quantitative values of relevant intermediate quantities are listed in Table 1 which will be filled in as the discussion proceeds.

An important parameter in the whistler regime is

$$g = \frac{\omega_{pe}^2}{\omega_{ce}^2} \tag{84}$$

and typically $g \gg 1$ in the whistler regime. The definition given by Eq.84 shows that g can depend on both density (via ω_{pe}^2) and on magnetic field (via ω_{ce}^2). In this paper we assume that the magnetic field is spatially uniform whereas the density is radially non-uniform so g depends only on the density profile.

The whistler regime is defined by the wave frequency being much higher than the lower hybrid frequency in which case ions make negligible contribution to the dielectric tensor elements which become

$$S = 1+\frac{g}{1-\bar{\omega}^2} \tag{85}$$

$$D = \frac{1}{\bar{\omega}}\frac{g}{(1-\bar{\omega}^2)} \tag{86}$$

$$P = 1-\frac{g}{\bar{\omega}^2} \tag{87}$$

$$R = 1+\frac{g}{\bar{\omega}(1-\bar{\omega})} \tag{88}$$

$$L = 1-\frac{g}{\bar{\omega}(1+\bar{\omega})}. \tag{89}$$

If $g \gg 1$, displacement current can also be neglected so the dielectric tensor elements further reduce to

$$S = \frac{g}{1-\bar{\omega}^2} \tag{90}$$

$$D = \frac{1}{\bar{\omega}}\frac{g}{(1-\bar{\omega}^2)} \tag{91}$$

$$P = -\frac{g}{\bar{\omega}^2} \tag{92}$$

$$R = \frac{g}{\bar{\omega}(1-\bar{\omega})} \tag{93}$$

$$L = -\frac{g}{\bar{\omega}(1+\bar{\omega})}. \tag{94}$$

To make the analysis more general, displacement current will be retained in the numerical calculations, as no additional effort is required to do so.

To relate to the Cartesian analysis in Section II, we note that for large $\bar{r}$ and uniform density, the cylindrical and Cartesian analyses are related by

$$N_z^2 = \frac{\bar{k}_z^2}{\bar{\omega}^2}g, \;\; N_r^2 = \frac{\bar{k}_x^2}{\bar{\omega}^2}g \tag{95}$$

where $\bar{k}_z$ and $\bar{k}_x$ are defined by Eqs.12 and 13. It can be demonstrated after a fair amount of algebraic manipulation that Eqs.4 and 74 (with displacement current neglected) are identical so any result derived using Eqs.4-20 also applies to Eq.74. In particular, the advantage of the Eq.18 representation is simplicity but this representation is only useful if the plasma has uniform density because distances are scaled to the electron skin depth d_e which depends on density. Thus, Eq.18 cannot be used for a plasma with a non-uniform density. The virtue of the Eq.74 representation is

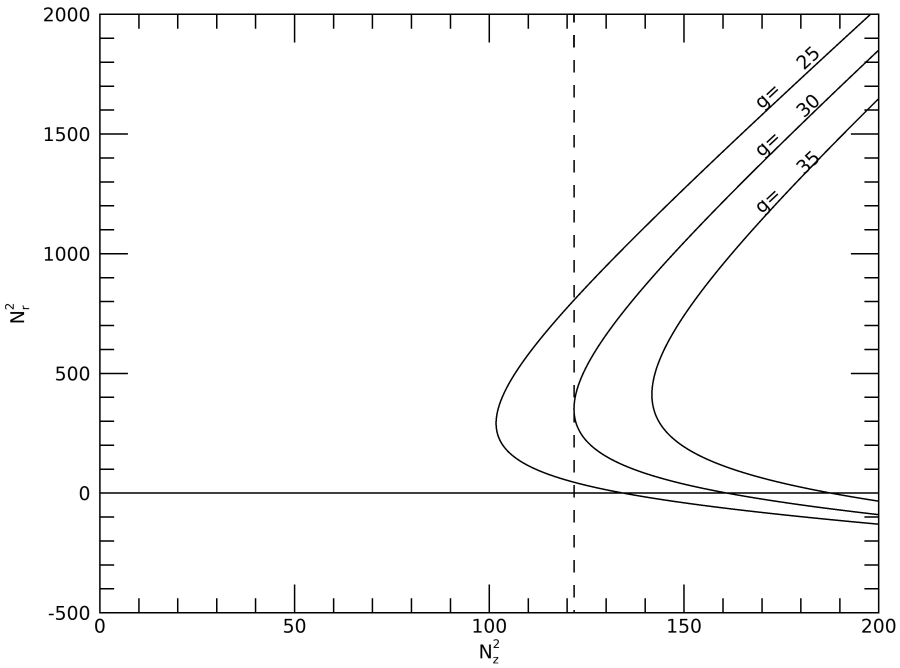

FIG. 1. Plot of N_r^2 versus N_z^2 from Eq.74 for three values of $g = \omega_{pe}^2/\omega_{ce}^2$.

that it is scaled to the vacuum wavelength which is independent of density and so can be used for a plasma with a non-uniform density. However, as will be discussed in Section XI, care is required when the frequency is varied because $\bar{r}$ depends on frequency.

Partial insight into the wave behavior is provided by Fig.1. This figure plots N_r^2 versus N_z^2 as determined by Eq.74 for $g = 25, 30$, and 35 and, for reference to the numerical calculation provided later, there is a dashed vertical line at the location where $N_z^2 = 121.742$. It is seen that the plot of N_r^2 intersects the dashed line at two locations for $g = 25$, at one location for $g = 30$ and at no locations for $g = 35$. The plasma is assumed to be uniform in the z direction so N_z is the same everywhere.

However, if the density depends on $\bar{r}$, then N_r will vary with $\bar{r}$ and so different $\bar{r}$ locations will

be associated with different curves in Fig.1. The up-slanting part of a curve in Fig.1 is called the slow mode (large N_r) and the down-slanting lower part is called the fast mode (small N_r).

To understand the structure of Eqs.63 and 64 we write these equations in a more compact form as

$$\mathscr{L}_\psi(\psi)+a_1\psi = b_1\chi \tag{96}$$

$$\mathscr{L}_\chi(\chi)+a_2\chi = b_2\psi. \tag{97}$$

where

$$a_1 = \frac{S^2-D^2}{S}-N_z^2 \tag{98}$$

$$b_1 = -N_z\frac{D}{S} \tag{99}$$

$$a_2 = P\left(1-\frac{N_z^2}{S}\right) \tag{100}$$

$$b_2 = -N_z\frac{DP}{S} \tag{101}$$

and

$$\mathscr{L}_\psi(\psi) = \frac{\partial^2\psi}{\partial\bar{r}^2}-\frac{1}{\bar{r}}\frac{\partial\psi}{\partial\bar{r}} \tag{102}$$

$$\mathscr{L}_\chi(\chi) = \frac{\partial^2\chi}{\partial\bar{r}^2}-\left(\frac{1}{\bar{r}}+\frac{1}{P}\frac{\partial P}{\partial\bar{r}}\right)\frac{\partial\chi}{\partial\bar{r}}. \tag{103}$$

The coefficients a_1, b_1, a_2, b_2 depend on S, P, and D which in turn depend on $\bar{r}$ via g. At this point, it is important to take into account that the density is a function of r rather than of $\bar{r}$ so adjustments will have to be made if $\bar{\omega}$ is changed. Combination of Eqs.10 and 38 shows that $r|\omega_{ce}|/c = \bar{r}/\bar{\omega}$.

For nominal terrestrial equatorial plane parameters at six Earth radii, $c/|\omega_{ce}| \approx 1000$ km which corresponds to the nominal width of whistler wave ducts reported in a statistical study by Gu et al.[28]. This indicates that $\bar{r}/\bar{\omega}$ will be of the order of unity at a duct edge.

To model a duct, we define ρ_1 as the value of $r|\omega_{ce}|/c$ at the start of the density rise from the duct bottom, ρ_2 as the value of $r|\omega_{ce}|/c$ at the conclusion of this density rise, and ρ_3 as a proxy for $\rho = \infty$. Since $\bar{r}$ rather than r is the independent variable in Eqs.102 and 103, it is necessary to express P and hence g as a function of $\bar{r}$ rather than as function of r. Using the ρ_1, ρ_2, ρ_3

definitions, the $g(\bar{r})$ profile is thus prescribed by

$$g(\bar{r}) = \begin{cases} g_{duct} & \text{for } 0 \le \bar{r} \le \bar{\omega}\rho_1 \\ g_{duct} + \frac{\Delta}{2}\left(1 + \sin\left(\frac{\pi}{\bar{\omega}(\rho_2-\rho_1)}\left(\bar{r} - \frac{\bar{\omega}(\rho_1+\rho_2)}{2}\right)\right)\right) & \text{for } \bar{\omega}\rho_1 \le \bar{r} \le \bar{\omega}\rho_2 \\ g_{duct} + \Delta & \text{for } \bar{\omega}\rho_2 \le \bar{r} \le \bar{\omega}\rho_3 \end{cases} \tag{104}$$

where g_{duct} denotes the value of g in the duct, Δ is the depth of the duct, the width of the transition region from inside the duct to outside is $\bar{\omega}(\rho_2 - \rho_1)$, and ρ_3 is a proxy for $\bar{r} = \infty$. This profile has $dg/dr = 0$ for both $\bar{r}/\bar{\omega} \le \rho_1$ and $\bar{r}/\bar{\omega} \ge \rho_2$. We choose $\rho_1 = 4$, $\rho_2 = 8$ and $\rho_3 = 40$. This definition of g has the necessary property that g has a fixed profile when plotted as a function of r. However, g will have an $\bar{\omega}$-dependent profile when plotted as a function of $\bar{r}$ because of the $\bar{\omega}$ -dependence of $\bar{r}$. Combination of Eqs.92 and 104 shows that

$$\frac{\partial P}{\partial \bar{r}} = \begin{cases} 0 & \text{for } 0 \le \bar{r} \le \bar{\omega}\rho_1 \\ -\frac{\Delta}{2\bar{\omega}^3}\left(\frac{\pi}{(\rho_2-\rho_1)}\cos\left(\frac{\pi}{\bar{\omega}(\rho_2-\rho_1)}\left(\bar{r} - \frac{\bar{\omega}(\rho_1+\rho_2)}{2}\right)\right)\right. & \text{for } \bar{\omega}\rho_1 \le \bar{r} \le \bar{\omega}\rho_2 \\ 0 & \text{for } \bar{\omega}\rho_2 \le \bar{r} \le \bar{\omega}\rho_3. \end{cases} \tag{105}$$

This expression is used in the evaluation of Eq.103.

Figure 2 plots g for $0 \le \bar{r}/\bar{\omega} \le 12$ for the situation where $\bar{\omega} = 0.25$. The region $12 \le \bar{r}/\bar{\omega} \le 40$ is not plotted as g is constant with the same value it has at $\bar{r}/\bar{\omega} = 12$; including this $12 \le \bar{r}/\omega \le 40$ region in the numerical computations is necessary for accuracy. The bottom horizontal axis in Fig. 2 is $\bar{r}$ which is frequency-dependent while the top horizontal axis is $\bar{r}/\bar{\omega}$ which is not frequency-dependent. The right-hand vertical axis shows $4g$ and indicates the predicted value of $N_z{}^2$ at the mode conversion location (neglecting the small effect of displacement current).

The g profile has two uniform-density regions smoothly joined by a transition region. These three regions have N_r^2 determined by the three curves in Fig.1. The virtue of having the uniform density $g = 25$ and $g = 35$ regions is that behavior in these regions can be quantitatively compared to the calculated predictions of uniform-density analytic models associated with Fig.1. The reason for having a smooth joining characterized by $dg/d\bar{r} = 0$ at ρ_1 and ρ_2 is to avoid sharp discontinuities that might cause reflections. The transition region must be examined numerically as the analytic models are based on the density being uniform.

To allow for a determination of parametric dependence, we will examine four situations; the first three situations are indicated in Fig.2. The first situation, called the reference situation, has $\bar{\omega} = 0.25$ and $\rho_{mc} = 6$ where the subscript 'mc' stands for 'mode conversion', i.e., the location where the fast and slow modes coalesce. The second and third situations also have $\bar{\omega} = 0.25$

	$0 \le \bar{r} \le 1$	$\bar{r} = 1.5$	$2 \le \bar{r} \le 10$	Equation reference
g	25	30	35	84,104
S	27.6667	33	38.3333	85
D	106.667	128	149.333	86
P	-399.0	-479	-559	87
N_{rs}^2	806.185	-	-	74,111
N_{rs}	28.3934			"
N_{rf}^2	45.2166	-	-	"
N_{rf}	6.72433	-	-	"
Γ	-	351.437	-	112
$\Gamma^{1/2}$	-	18.7467	-	"
a_1	-	-	-665.159	98
b_1	-	-	-42.9833	99
a_2	-	-	1216.31	100
b_2	-	-	24027.7	101
α	-	-	473.02	126
β	-	-	0.9488856	127
N_t	-	-	19.3468	132
κ_t	-	-	9.93588	133
η	-	-	23.6432	137
δ	-	-	-0.387962	138

TABLE I. Parameters relevant for comparing with the reference situation numerical solution using $N_z^2 = 121.742$ and $\bar{\omega} = 0.25$, $\bar{\omega}\rho_1 = 1$, $\bar{\omega}\rho_{mc} = 1.5$, $\bar{\omega}\rho_2 = 2$, $\bar{\omega}\rho_3 = 10$.

but now have $\rho_{mc} = 5$ and $\rho_{mc} = 7$ respectively to reveal the dependence on ρ_{mc}. Since Eq.9 showed that at the mode conversion location $N_z{}^2 = 4g$ (neglecting displacement current), showing this dependence on ρ_{mc} is tantamount to showing the dependence on $N_z{}^2$ (see right hand scale of Fig.2). The fourth situation has $\rho_{mc} = 6$ as in the reference situation but now has $\bar{\omega} = 0.20$ to show the dependence on frequency. The reference situation will be discussed in this section. Because of the length and complexity of this discussion, the discussion of situations two, three, and four will be deferred to Sec.XI.

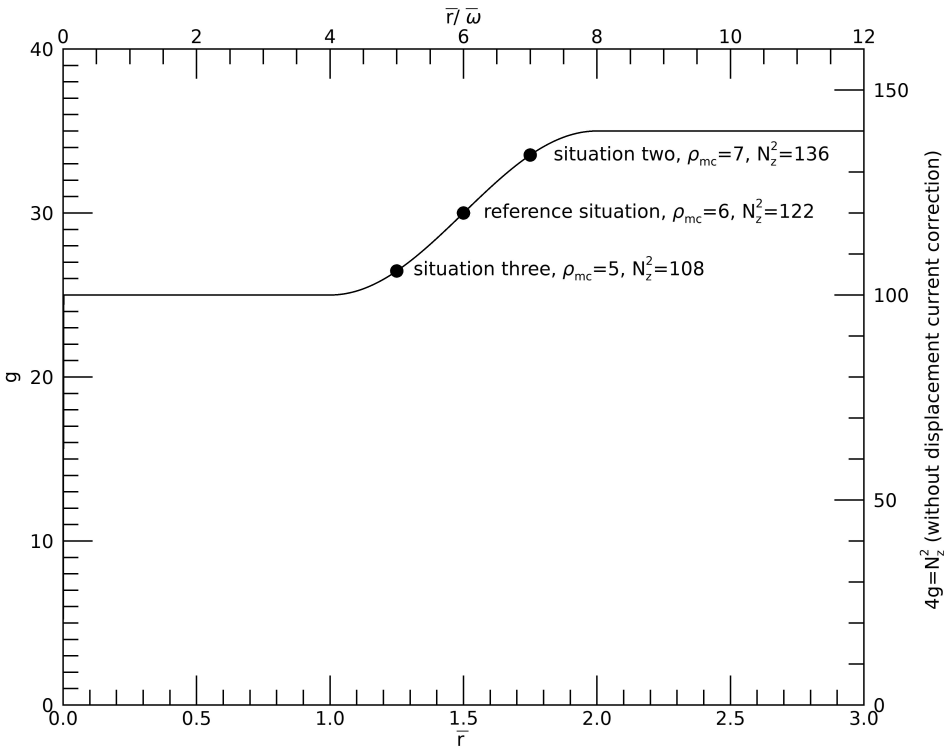

FIG. 2. Plot of $g(\bar{r})$ as prescribed by Eq. 104 for $\bar{\omega} = 0.25$. The values of N_z^2 are calculated using Eq. 117, and are approximately given by $N_z^2 = 4g(r_{mc})$ (see Eqs.9 and 120).

Using $\rho_{mc} = 6$ gives $\bar{r}_{mc} = \bar{\omega}\rho_{mc} = 1.5$ and $g(\bar{r}_{mc}) = 30$. Thus Eqs.85, 86 and 87 give $S = 33$, $D = 128$, and $P = -479$ at $\bar{r} = \bar{r}_{mc}$.

The four boundary conditions for the fourth order system comprised by Eqs.96 and 97 are (i) both ψ, χ scale as $\bar{r}^2$ for small $\bar{r}$ and (ii) both ψ, χ decay exponentially to zero at large $\bar{r}$. It is thus not feasible to start the numerical integration of Eqs.96 and 97 at $\bar{r} = 0$ because such an integration would require nontrivial Neumann or nontrivial Dirichlet boundary conditions but regularity requires both $\psi = \chi = 0$ at $\bar{r} = 0$ and $d\psi/d\bar{r} = d\chi/d\bar{r} = 0$ at $\bar{r} = 0$. Similarly, it is not feasible to start the integration at some large value of $\bar{r}$ used as a proxy for infinity. To overcome these issues, the $\bar{r}$ domain is divided into an inner and an outer region where $\bar{r}_{mc}$ defines the

boundary between these two regions.

Boundary conditions for the inner region are specified at $\bar{r} = 0$ and at $\bar{r}_{mc}$. Boundary conditions for the outer region are specified at $\bar{r}_{mc}$ and at $\bar{r} = \rho_3\bar{\omega}$ which serves as a proxy for infinity. Equations 63 and 64 are written in a form suitable for use in the code described in Bellan[38] which provides a single-pass method for solving these types of equations using boundary conditions on ψ and χ at the inner and outer boundaries of an $\bar{r}$ domain. The location $\bar{r}_{mc}$ is defined to be where

$$\psi^{-1}\mathscr{L}_{\psi}(\psi) = -\Gamma^2 \tag{106}$$

$$\chi^{-1}\mathscr{L}_{\chi}(\chi) = -\Gamma^2 \tag{107}$$

and Γ^2 corresponds to the two roots of N_r^2 being identical at $\bar{r}_{mc}$ where the fast and slow modes coalesce. At $\bar{r}_{mc}$ Eqs.96 and 97 become

$$\left(-\Gamma^2 + a_1\right)\psi \;=\; b_1\chi \tag{108}$$

$$\left(-\Gamma^2 + a_2\right)\chi \;=\; b_2\psi. \tag{109}$$

Multiplying the left sides of these equations by the right hand sides gives the quadratic equation in Γ^2

$$\Gamma^4 - \Gamma^2(a_1 + a_2) + a_1a_2 - b_1b_2 = 0 \tag{110}$$

which is the same as Eq.74 with $N_r^2 \to \Gamma^2$ but has a subtly different interpretation. Equation Eq.74 described a set of uniform plasmas having different densities whereas Eq.110 describes a specific single plasma with a spatially varying density. The two solutions of Eq.111 are

$$\Gamma^2 = \frac{(a_1 + a_2) \pm \sqrt{(a_1 - a_2)^2 + 4b_1b_2}}{2}. \tag{111}$$

The situation can be understood by supposing that Γ^2 is also defined away from the mode conversion location and so is the same as N_r^2 in Eq.74. Using this WKB point of view shows that for $\bar{r} < \bar{r}_{mc}$ there are distinct fast and slow modes and that these merge at $\bar{r} = \bar{r}_{mc}$.

For $\bar{r} > \bar{r}_{mc}$, N_r^2 is complex. Figure 3 shows a plot of these modes and shows that to the left of the mode conversion location, the slow mode N_r^2 (red, + chosen in Eq.111) is pure real and much larger than the fast mode N_r^2 (green, − chosen in Eq.111). The situation is very different in the outer region, $\bar{r} > \bar{r}_{mc}$ as now N_r^2 is complex. The real parts of what were the slow and fast modes now have identical value, and the imaginary part of what was the slow mode on the left is positive (cyan) while the imaginary part of what was the fast mode on the left is now negative (blue). For

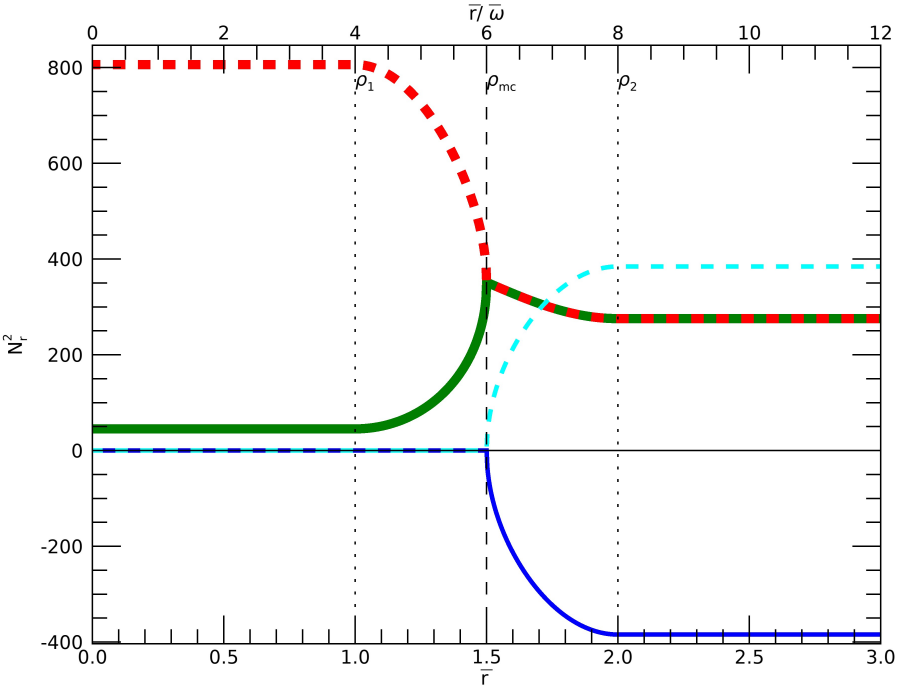

FIG. 3. Plot of N_r^2 versus position assuming that at each position the plasma is uniform; reference situation parameters are used, i.e., $\bar{\omega} = 0.25$ and $\rho_{mc} = 6$ so $\bar{r}_{mc} = 1.5$. The assumption that the plasma is uniform is true for $0 < \bar{r} < \omega\rho_1$ and for $\rho_2\bar{\omega} < \bar{r}$ but not for $\rho_1 < \bar{r}/\bar{\omega} < \rho_2$ which is where a numerical solution is essential. However, despite not being accurate in this intermediate region, the plot gives some intuition regarding the wave behavior and shows that the fast and slow modes merge at $\bar{r}_{mc} = \bar{\omega}\rho_{mc}$.

completeness, these blue and cyan lines are also shown on the left and are at zero, indicating that N_r^2 is pure real for both modes in this region.

At $\bar{r}_{mc}$ where $S = 33, D = 128$, $P = -479$ the term involving the square root vanishes so the $\pm$ solutions are identical in Eq.111 and are denoted by

$$\Gamma_{mc}^2 = \frac{a_1 + a_2}{2}. \tag{112}$$

Equation 109 shows that at $\bar{r} = \bar{r}_{mc}$

$$\frac{\chi}{\psi} = \frac{b_2}{-\Gamma_{mc}^2 + a_2} = \frac{2b_2}{a_2 - a_1}. \tag{113}$$

The requirement that the square root term in Eq.111 vanishes implies that

$$(a_1 - a_2)^2 + 4b_1 b_2 = 0 \tag{114}$$

which on substituting for a_1, b_1, a_2, B_2 becomes

$$\left(\left(S\left(S - N_z^2\right) - D^2\right) - P\left(S - N_z^2\right)\right)^2 + 4N_z^2 D^2 P = 0. \tag{115}$$

Equation 115 is a quadratic equation in N_z^2 with the two roots

$$N_z^2 = \frac{(P-S)^2 S - (P+S)D^2 \pm 2D\sqrt{PS\left(D^2 - (P-S)^2\right)}}{(P-S)^2}. \tag{116}$$

The positive sign choice corresponds to $N_z^2 \gg 1$ which is the root of interest while the negative sign gives $N_z^2 \ll 1$ which is not of interest. Hence we choose

$$N_z^2 = \frac{(P-S)^2 S - (P+S)D^2 + 2D\sqrt{PS\left(D^2 - (P-S)^2\right)}}{(P-S)^2}. \tag{117}$$

Equation 117 gives $N_z^2 = 121.742$, close to the value $4g_{mc}$ predicted by Eq.9, the slight difference resulting from the inclusion of displacement current in the definitions of S and P. This gives $N_z = 11.0337$. Because the negative sign choice gives $N_z^2 \approx 0$, the magnitude of the square root term is nearly equal to the other term in the numerator, that is

$$2D\sqrt{PS\left(D^2 - (P-S)^2\right)} \simeq (P-S)^2 S - (P+S)D^2 \tag{118}$$

so

$$N_z^2 \simeq 2S - 2\frac{(P+S)D^2}{(P-S)^2}. \tag{119}$$

If displacement current is ignored and Eqs. 90-92 are used, Eq.119 reduces to

$$N_z^2 = 4g_{mc} \tag{120}$$

which corresponds to Eq.9. This shows again that for a ducting situation, N_z^2 is determined by the plasma parameters at the mode conversion location in the duct. In the analysis presented here the

location of the mode conversion is specified and the corresponding N_z^2 is calculated. One could invert this approach by specifying N_z^2 and then use Eq.120 to determine the density and hence location of the mode conversion. On taking into account the g profile and hence density profile in Fig.2, Eq.120 indicates that N_z^2 could range from 100 to 140 since g ranges from 25 to 35. The mode conversion location would then be at the location in Fig.2 where Eq.120 is satisfied.

Consider the region $\bar{r} \geq \rho_2 \bar{\omega}$. By having $dg/dr = 0$ at $\bar{r} = \rho_2$, the uniform plasma solution is valid at this location and there are no discontinuities in any derivatives so all quantities should be continuous at this location.

In the $\bar{r} \geq \rho_2 \bar{\omega}$ region, $g = 35$ and the dielectric tensor elements now have the values $S = 38.3333$, $D = 149.333$ and $P = -559$ and are uniform. This uniformity means that Γ can be interpreted as being a uniform N_r^2 so Eq.111 can be written as

$$N_r^2 = \frac{(a_1 + a_2) \pm \sqrt{(a_1 - a_2)^2 + 4 b_1 b_2}}{2} \tag{121}$$

where again the solutions ψ, χ are of the form $\bar{r} J_1(N_r \bar{r})$. However, in this region $\sqrt{(a_1 - a_2)^2 + 4 b_1 b_2}$ is imaginary so Eq.121 can be expressed as

$$N_r^2 = W \pm iH \tag{122}$$

where

$$W = \frac{a_1 + a_2}{2} \tag{123}$$

$$H = \frac{\sqrt{-(a_1 - a_2)^2 - 4 b_1 b_2}}{2}. \tag{124}$$

Equation 121 can be expressed in a form suitable for later taking a square root, namely as

$$\begin{aligned} N_r^2 &= \alpha \left(\frac{W}{\sqrt{W^2 + H^2}} + (-1)^p i \frac{H}{\sqrt{W^2 + H^2}} \right) \\ &= \alpha \exp\left(i (-1)^p \beta \right) \end{aligned} \tag{125}$$

where $p = 1, 2$ and

$$\alpha = \sqrt{W^2 + H^2} \tag{126}$$

$$\beta = \tan^{-1}(H/W). \tag{127}$$

Taking the square root gives

$$N_r = (-1)^q \alpha^{1/2} \exp\left(i (-1)^p \beta / 2 \right) \tag{128}$$

where $q = 0,1$. There are thus four possible solutions given by $\{p,q\} = \{1,1\}$, $\{1,0\}$, $\{0,1\}$, $\{0,0\}$. Numerical values of $a_1, b_1, a_2, b_2, W, H, \alpha, \beta$ are listed in the $\rho_2 \le \bar{r} \le \bar{r}_{max}$ column of Table 1.

Solutions that vanish at infinity require the imaginary part of N_r to be positive and so are restricted to the solutions having $\{p,q\} = \{0,0\}, \{1,0\}$, that is

$$N_r = +\alpha^{1/2}\cos(\beta/2) + i\alpha^{1/2}\sin(\beta/2) \tag{129}$$

$$N_r = -\alpha^{1/2}\cos(\beta/2) + i\alpha^{1/2}\sin(\beta/2). \tag{130}$$

The real parts of these two solutions have equal magnitudes but opposite signs while the imaginary parts have equal magnitudes and the same signs. If cylindrical geometry effects are neglected, the solution has an $\exp(iN_r\bar{r})$ dependence. If cylindrical geometry effects are included, then the solution will be the form of a Bessel function having complex argument. Since the Bessel function and $\exp(iN_r\bar{r})$ dependence become similar at large $\bar{r}$ as cylindrical geometry effects become small, we will consider the $\exp(iN_r\bar{r})$ approximation which is more easily understood. Because ψ and χ are assumed to be real, they each must be a linear combination of $\cos\left(\alpha^{1/2}\cos(\beta/2)\,\bar{r}\right)e^{-\alpha^{1/2}\sin(\beta/2)\bar{r}}$ and $\sin\left(\alpha^{1/2}\cos(\beta/2)\,\bar{r}\right)e^{-\alpha^{1/2}\sin(\beta/2)\bar{r}}$. This means that the solution for ψ in the $\rho_2 \le \bar{r} \le \bar{r}_{max}$ region must be of the form

$$\psi(\bar{r}) = \psi_0\cos(N_t(\bar{r}-\bar{r}_0))e^{-\kappa_t(\bar{r}-\bar{r}_0)} \tag{131}$$

where $\psi = \psi_0$ at $\bar{r} = \bar{r}_0$ with tunneling coefficients denoted by subscript 't' given as

$$N_t = \mathrm{Re}(N_r) = \alpha^{1/2}\cos(\beta/2) \tag{132}$$

$$\kappa_t = \mathrm{Im}(N_r) = \alpha^{1/2}\sin(\beta/2)). \tag{133}$$

Thus, N_t is the refractive index (normalized wave number) and κ_t is the exponential decay rate of a spatially oscillating, decaying ψ in the region $\rho_2 \le \bar{r} \le \bar{r}_{max}$.

Because cylindrical geometry terms are being neglected, Eq.96 can be written

$$\chi(\bar{r}) = \frac{1}{b_1}\left(\frac{\partial^2\psi}{\partial\bar{r}^2} + a_1\psi\right). \tag{134}$$

Evaluating $\partial^2\psi/\partial\bar{r}^2$ using Eq.131 for ψ gives

$$\frac{\partial^2\psi}{\partial\bar{r}^2} = \psi_0\left[\left(\kappa_t^2 - N_t^2\right)\cos(N_t(\bar{r}-\bar{r}_0)) + 2N_t\kappa_t\sin(N_t(\bar{r}-\bar{r}_0))\right]e^{-\kappa_t(\bar{r}-\bar{r}_0)}. \tag{135}$$

Using Eq.135 in Eq.134 gives

$$\chi(\bar{r}) = \eta\,\psi_0 \cos\left(N_t\left(\bar{r}-\bar{r}_0\right)-\delta\right) e^{-\kappa_t(\bar{r}-\bar{r}_0)} \tag{136}$$

where

$$\eta \;=\; \sqrt{\frac{\left(\kappa_t^2 - N_t^2 + a_1\right)^2 + 4\kappa_t^2 N_t^2}{b_1^2}} \tag{137}$$

$$\delta \;=\; \tan^{-1}\frac{2\kappa_t N_t}{\kappa_t^2 - N_t^2 + a_1}. \tag{138}$$

The numerical values in Table 1 give $\eta = 23.6432$ and $\delta = -0.387962$. This value of δ indicates that the phase of χ should lead the phase of ψ by $|\delta|/2\pi = 0.06$ wavelengths.

X. NUMERICAL SOLUTION

A. Numerical solution: results

Equations 96 and 97 are solved numerically. Results of this numerical solution are presented in Fig.4. We discuss features of this figure in this subsection, then in the next subsection discuss the rather intricate details of the numerical method, and then in a following subsection demonstrate that the numerical solutions are valid. The discussions of the numerical method reveal an important issue that at first appears to be a purely numerical problem, but then is realized to be associated with a failure of the Eq.1 plane wave assumption in the vicinity of the mode conversion layer. It is shown that Eq.1 omits a required new type of solution that is intrinsic to the fourth-order nature of the system.

Figure 4 plots $\psi(\bar{r})$, and $\chi(\bar{r})$ normalized to their values at $\bar{r} = 1.5$ with $\psi = 1$ at $\bar{r} = 1.5$. It shows that $\psi, \chi \to 0$ at $r = 0$ and at $\bar{r} \to \infty$. The numerical solutions (solid black and green lines) are fit to Bessel function solutions in the region $0 \le \bar{r} \le \rho_1$ where the density is uniform as prescribed by Eq.104 and shown in Fig.2. The fitted solution for ψ is determined by assuming $\psi(\bar{r}) = \bar{r}\left(c_1 J_1(N_{rs}\bar{r}) + c_2 J_1(N_{rf}\bar{r}\right) + \tilde{c}_1 Y_1(N_{rs}\bar{r}) + \tilde{c}_2 Y_1(N_{rf}\bar{r}))$ and then solving for the four coefficients $c_1, c_2, \tilde{c}_1, \tilde{c}_2$ by using the numerical solution to give ψ at 4 different values of $\bar{r}$ so as to have four equations in four unknowns. Solution of this system of four equations shows that the coefficients $\tilde{c}_1, \tilde{c}_2$ of the Y_1 Bessel functions are negligible as expected (see first paragraph of Section V). The function $\bar{r}\left(c_1 J_1(N_{rs}\bar{r}) + c_2 J_1(N_{rf}\bar{r})\right)$ is plotted as the dashed red line in Fig.2. It

is seen that this dashed red line lies on top of the black line showing that in the region $0 \leq \bar{r} \leq \rho_1$ the numerical solution is, as expected, a sum of a slow and a fast wave where each has a Bessel function dependence. A similar process shows that χ is also a sum of a slow and a fast Bessel function in the $0 \leq \bar{r} \leq \rho_1$ region. These solutions in the $0 \leq \bar{r} \leq \rho_1$ region are the sum of a short wavelength solution (slow mode) and a long wavelength solution (fast mode) as seen by the short wavelength waves riding on the long wavelength wave.

Figure 4 shows that on approaching $\bar{r} = 1.5$, there is no longer a short wavelength wave riding on a long wavelength wave, but instead there is only one wavelength for both ψ and χ and this wavelength is intermediate between the short and long wavelengths seen in the $0 \leq \bar{r} \leq \rho_1$ region.

Figure 4 also plots $4000\psi e^{9.7(\bar{r}-2.4)}$ in the range $2.4 \leq \bar{r} \leq 3$ as a dotted black line and shows that in this region ψ is both spatially oscillating and exponentially decaying. Similarly, Fig. 4 also plots $200\chi e^{9.7(\bar{r}-2.4)}$ in the range $2.4 \leq \bar{r} \leq 3$ as a dashed green line. Using the numerical values listed in Table 1 and Eqs.132,133 it is seen that the predicted wavenumber is $N_t = 19.3$ and the predicted spatial exponential decay rate is $\kappa_t = 9.93$. The constant amplitude of these plots show that ψ and χ are decaying by a factor $e^{-9.7\bar{r}}$ which is in good agreement with the $\kappa_t = 9.93$ predicted by Eq.133. As shown by the horizontal blue arrow at the top right of Fig. 4 the wavelength of these ψ and χ plots is 0.32 corresponding to a wavenumber $2\pi/0.32 = 19.6$ which is in good agreement with the predicted $N_t = 19.3$. Thus, the wavelength and spatial decay rate determined from the $\bar{r} > 2.4$ region of Fig.4 agree reasonably well with the analytic model predictions, the small discrepancies presumably resulting from neglecting cylindrical geometry terms of order $1/\bar{r}$ in Eqs.132,133. Furthermore, in agreement with Eq.138 it is seen that the phase of χ leads the phase of ψ by 0.07 wavelengths, i.e., by $\Delta\bar{r} = 0.02$. The fact that the magnified plots of ψ and χ shown as dotted and dashed lines on the right of Fig. 4 have a relative magnification ratio $\chi/\psi = 4000/200 = 20$ and appear in the plot with a χ/ψ amplitude ratio of 1.17 indicates that $\chi/\psi \simeq 23.4$ which is consistent with $\eta = 23.64$ where η is given by Eq.137.

Figures 5 and 6 provide checks on the validity of the numerical solution. These are plots of the numerically calculated ψ and χ substituted into Eqs.96 and 97. The left hand side of these equations is plotted as a black line and the right hand side is plotted as a dashed red line. The observed overlay of the dashed red line on the black line indicates that the right hand side equals the left hand side and so shows that the equations have been solved.

Figures 7 and 8 show the electric and magnetic field components calculated from ψ and χ using Eq.65.

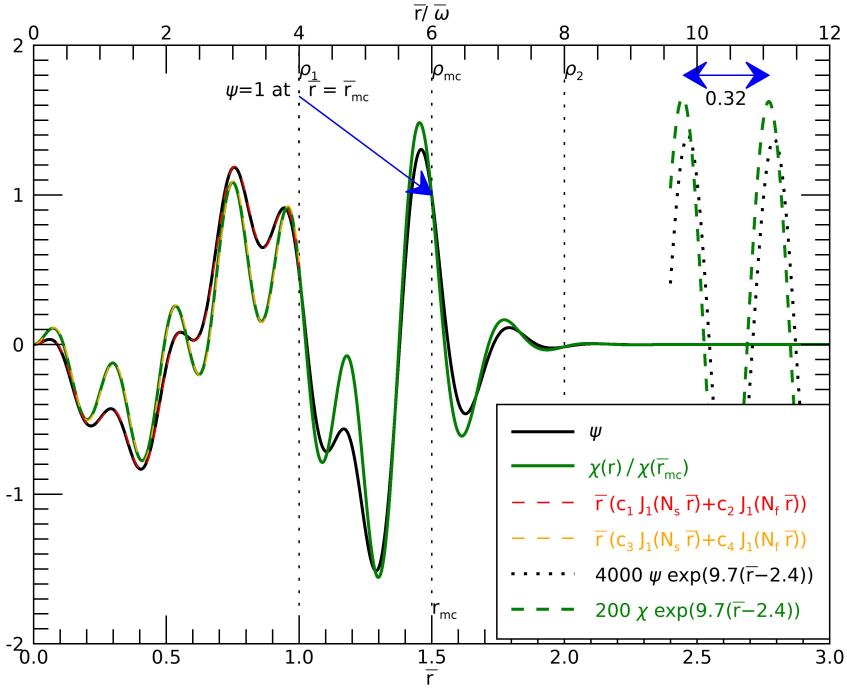

FIG. 4. Numerical solution of Eqs.96 and 97 for reference situation ($\bar{\omega} = 0.25$, $\rho_1 = 4$, $\rho_{mc} = 6$, $\rho_2 = 8$, $\rho_3 = 40$). The black and green lines show ψ and χ normalized to their respective values at $\bar{r} = \bar{r}_{mc} = 1.5 = \bar{\omega}\rho_{mc}$. The dashed red and orange lines show Bessel solutions with coefficients chosen to match the numerical solution in the uniform density $0 \leq \bar{r} \leq 1$ region. The dotted black line and dashed green line indicate that ψ and χ have a spatial periodicity and rate of decay consistent with analytic model predictions in the $2 \leq \bar{r} \leq 3$ region.

B. Summary of numerical method

The boundary conditions that ψ, χ, $\partial\psi/\partial\bar{r}$ and $\partial\chi/\partial\bar{r}$ all vanish at $\bar{r} = 0$ and at $\bar{r} = \infty$ means that the equations cannot be solved by starting an integration at the boundaries. Instead of integrating from the boundaries, a numerical method is used that is a form of the 'shoot first and then

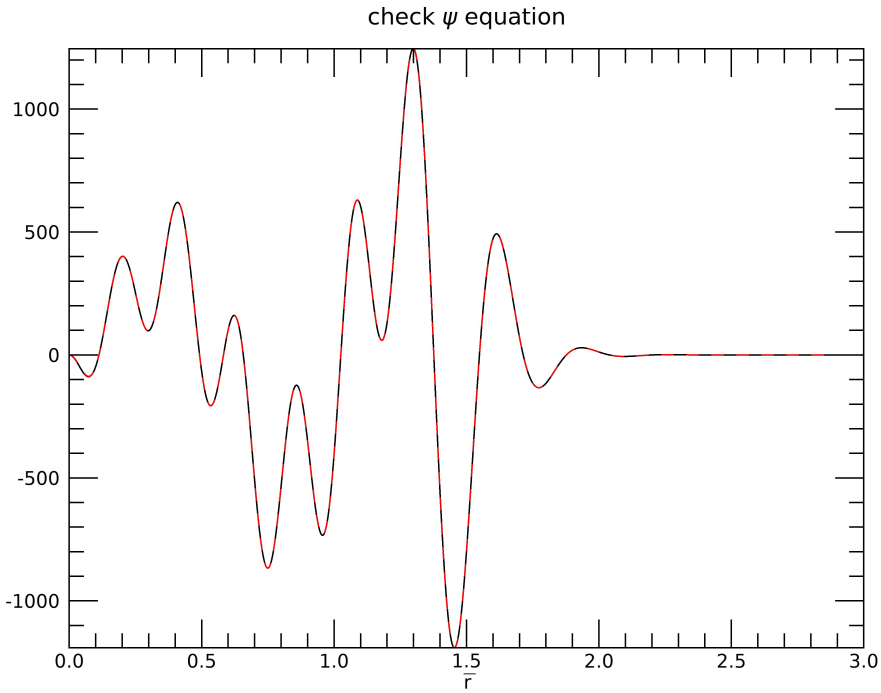

FIG. 5. Black line shows numerical solution for numerically calculated ψ substituted into the left hand side of Eq.96 and dashed red line shows right hand side of this equation using calculated χ.

relax later' strategy advocated in Section 18.0 of Press *et al.* [39]. The method is summarized as:

1. A large value of $\bar{r}_{max}$ is chosen to serve as a proxy for infinity. The domain from $\bar{r} = 0$ to $\bar{r} = \bar{r}_{max}$ is discretized into $N = 4000$ equal steps separated by $\Delta_r = \bar{r}_{max}/N$. The discrete values of $\bar{r}$ are labeled by $j = 0, N$. The mode conversion location is at the step $j = M$ where $M = N\bar{r}_{mc}/\bar{r}_{max}$ where $\bar{r}_{mc}$ is the location of the mode conversion. The value of ψ at position $\bar{r} = j\Delta_r$ will be denoted ψ_j and similarly for χ.

2. An error metric ε is defined, the minimization of which corresponds to having a better solution to Eqs.63 and 64.

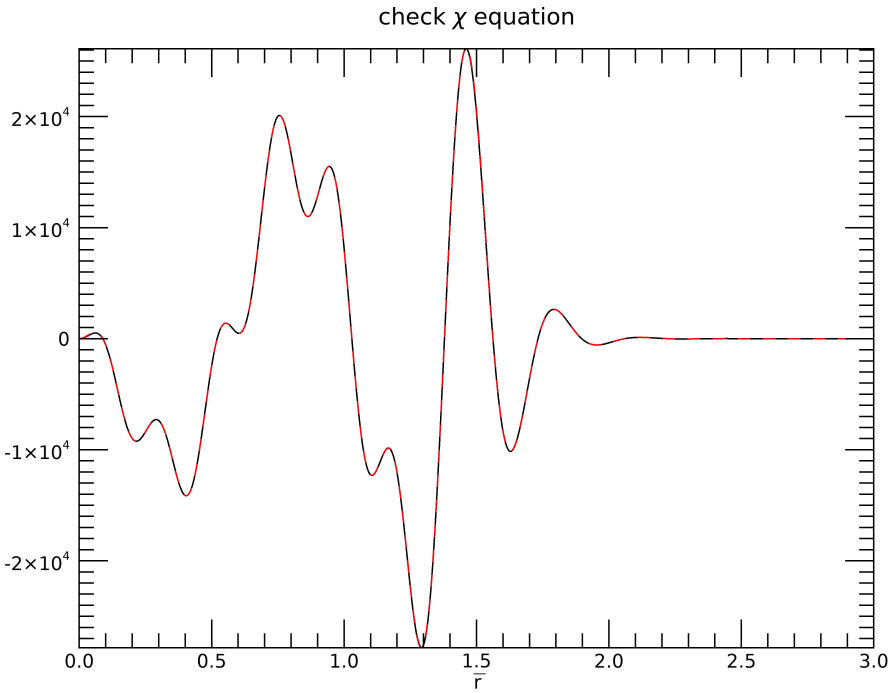

FIG. 6. Black line shows numerical solution for χ substituted into the left hand side of Eq.97 and dashed red line shows right hand side using calculated ψ.

3. Because the problem is linear, ψ_M is set to be unity and maintained at this value throughout the calculation.

4. A first guess for χ_M is prescribed by Eq.113.

5. The method described in Bellan[38] is used to solve Eqs.63 and 64 in the inner subdomain from $j = 0$ to $j = M$.

6. It is assumed that $\partial^2\psi/\partial\bar{r}^2$ and $\partial^2\chi/\partial\bar{r}^2$ change very little when $j \to j+1$ so that the values of these second derivatives at $j = M$ can be estimated using their values at $j = M-1$.

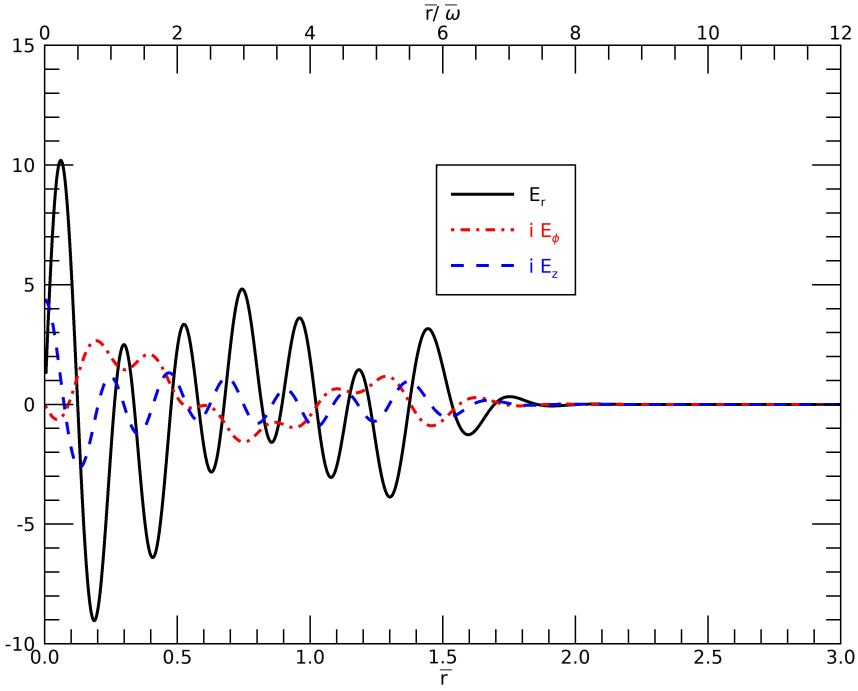

FIG. 7. Electric field components calculated using Eq.65

7. These estimated second derivatives are used to calculate estimated values for ψ_{M+1} and χ_{M+1} and these values provide the inner boundary conditions for the outer subdomain which spans from $j = M+1$ to $j = N$. The method described in Bellan[38] is used to solve Eqs.63 and 64 in the outer subdomain.

8. It is found that this method produces significant spikes in derivatives of ψ and χ at $j = M$ and at $j = M+1$ and the magnitude of these spikes depends on the value assumed for χ_M. A shooting method is used to find the χ_M that minimizes the error metric ε. Equation 113 provides the initial guess for χ_M. Figure 9 shows the variation of ε with χ_M and that ε has a minimum when χ_M is approximately 86 percent of the value prescribed by Eq.113. This minimum value of ε corresponds to minimization of the spikes in ψ and χ at $j = M$ and at

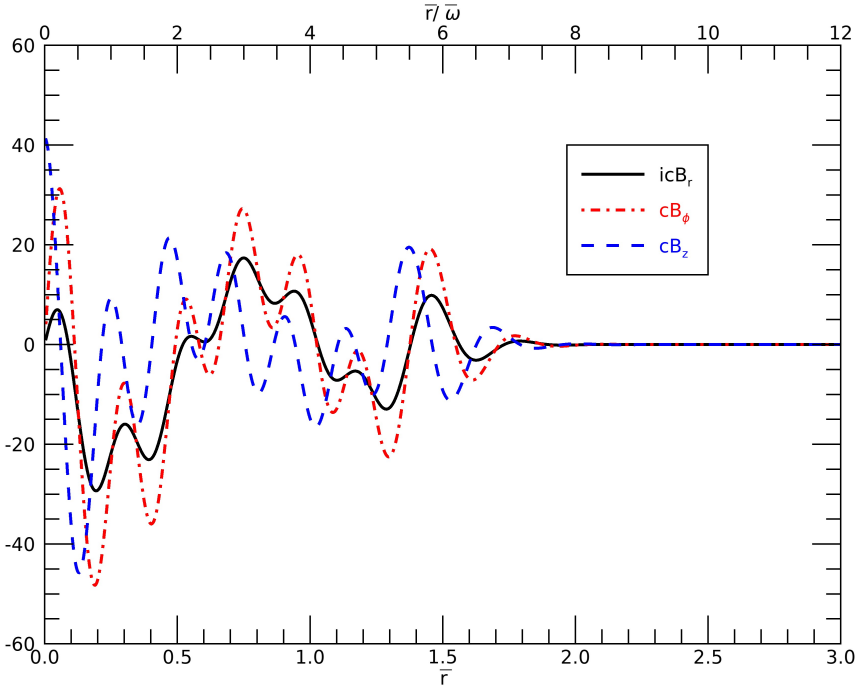

FIG. 8. Magnetic field components calculated using Eq.65

$j = M+1$. Although the spikes are minimized, they are unacceptably large.

9. To further reduce the spikes, a relaxation procedure is used that begins with the results of the shooting method in steps 1-8. This relaxation procedure maintains $\psi_M = 1$ but otherwise repeatedly recalculates ψ_j and χ_j for all other $0 < j < N$. Each recalculation uses information from nearest neighbors in a discretized form of Eqs.63 and 64. This relaxation reduces ε from 0.18 to about 0.018 in about 10^2 relaxation steps so that the spikes are no longer visible. Plots (see Figs. 5,6) show there is no difference between the left and right hand sides of each of Eqs.63 and 64 so these equations are deemed to be solved.

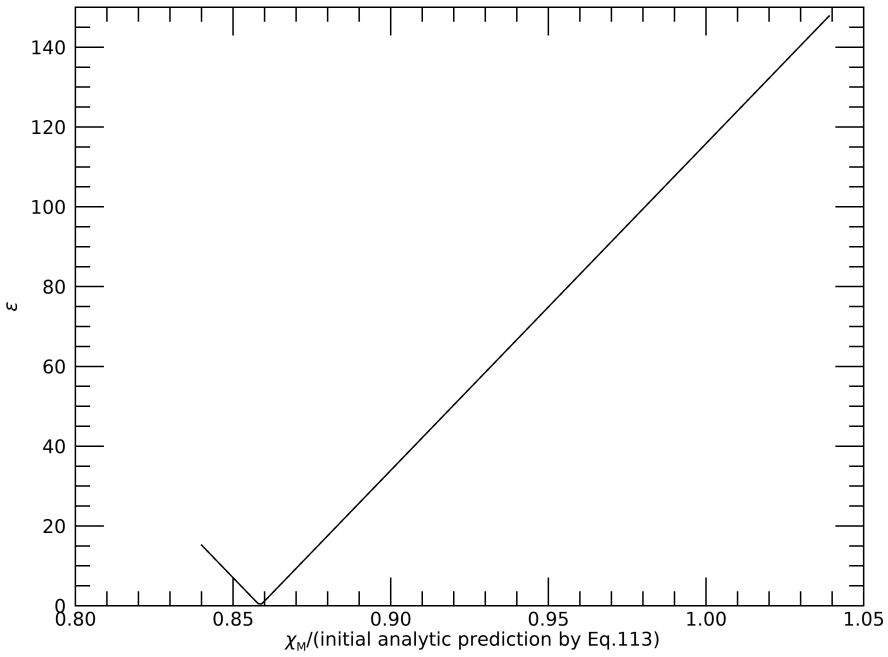

FIG. 9. Dependence of ε on guess for χ_M for reference situation. The value of χ_M that minimizes ε is different for each of situations reference, two, three, and four.

C. Details of numerical method

The following fixed prescriptions are made:

1. $\psi_0 = 0$, $\chi_0 = 0$,$\psi_N = 0$, $\chi_N = 0$
2. $\psi_M = 1$,
3. initially χ_M is prescribed by Eq. 113 but then χ_M is repeatedly recalculated as the solution proceeds.

Using these boundary conditions Eqs. 63 and 64 are solved in the inner subdomain from $j = 0$ to

$j = M$.

The inner boundary conditions for the outer subdomain are next determined. The second order difference operator $\partial^2\psi/\partial\bar{r}^2 = (\psi_{j+1} + \psi_{j-1} - 2\psi_j)/\Delta_r^2$ is used to calculate $\partial^2\psi/\partial\bar{r}^2$ at location $j = M-1$. The inner subdomain solution provides ψ_{M-2}, ψ_{M-1} and ψ_M. It is then assumed that $\partial^2\psi/\partial\bar{r}^2$ has nearly the same value at $j = M$ and is used estimate ψ_{M+1} using ψ_{M-1} and ψ_M. The same procedure is followed to obtain χ_{m+1}. These values of ψ_{M+1} and χ_{M+1} are used as the inner boundary conditions for the outer subdomain. The method described in Bellan[38] is now used to solve Eqs.63 and 64 in the outer subdomain from $j = M+1$ to $j = N$.

Using the definitions given by Eqs.102,103 the error metric is defined as

$$\varepsilon = \sqrt{\sum_{j=M}^{M+1}\left(\begin{array}{c}\left(\left[\psi - \frac{b_1}{a_1}\chi + \frac{1}{a_1}\bar{r}\,\frac{\partial}{\partial r}\left(\frac{1}{\bar{r}}\frac{\partial\psi}{\partial r}\right)\right]_j\right)^2 \\ +\left(\left[\psi - \frac{a_2}{b_2}\chi - \frac{\bar{r}P}{b_2}\frac{\partial}{\partial r}\left(\frac{1}{rP}\frac{\partial\chi}{\partial r}\right)\right]_j\right)^2\end{array}\right)}. \tag{139}$$

This definition has the properties that (i) $\varepsilon = 0$ if Eqs.63 and 64 are satisfied at $j = M$ and at $j = M+1$ and (ii) $\varepsilon \geq 0$. To the extent that the solution is nearly exact, ε will be a positive number much less than unity since ε has been constructed from the difference between quantities that are of the order of unity, namely ψ minus the rest of the terms in the differential equations. The shooting method for finding the minimum of ε consists of defining a function $\partial\varepsilon/\partial\chi_M$ as a function of χ_M and then using a Newton-Raphson method[39] to find the χ_M that is the root of this function. The solutions for ψ and χ associated with this ε-minimizing choice of χ_M provide the initial guess for the relaxation scheme.

The relaxation scheme is constructed by writing Eqs.96 and 97 in difference form as

$$\frac{\psi_{j+1} + \psi_{j-1} - 2\psi_j}{\Delta^2} - \frac{1}{j\Delta}\frac{\psi_{j+1} - \psi_{j-1}}{2\Delta} = b_1\chi_j - a_1\psi_j \tag{140}$$

$$\frac{\chi_{j+1} + \chi_{j-1} - 2\chi_j}{\Delta^2} - \frac{1}{j\Delta}\left(1 + \frac{\bar{r}}{P}\frac{\partial P}{\partial\bar{r}}\right)\frac{\chi_{j+1} - \chi_{j-1}}{2\Delta} = b_2\psi_j - a_2\chi_j. \tag{141}$$

.

We define

$$a_1^* = a_1 - \frac{2}{\Delta^2} \tag{142}$$

$$a_2^* = a_2 - \frac{2}{\Delta^2} \tag{143}$$

$$\nu = 1 + \frac{\bar{r}}{P}\frac{\partial P}{\partial\bar{r}} \tag{144}$$

and

$$s_1 = \frac{\psi_{j+1} + \psi_{j-1} - \frac{1}{2j}\left(\psi_{j+1} - \psi_{j-1}\right)}{\Delta^2} \tag{145}$$

$$s_2 = \frac{\chi_{j+1} + \chi_{j-1} - \frac{\nu}{2j}\left(\chi_{j+1} - \chi_{j-1}\right)}{\Delta^2}. \tag{146}$$

Solving Eqs.140 and 141 for new ψ_j and new χ_j in terms of values of nearest neighbors then gives

$$\psi_j^{new} = -\frac{s_2 b_1 + s_1 a_2^*}{a_1^* a_2^* - b_1 b_2}, \tag{147}$$

$$\chi_j^{new} = -\frac{s_1 b_2 + s_2 a_1^*}{a_1^* a_2^* - b_1 b_2}. \tag{148}$$

Each step in the relaxation procedure consists of calculating new ψ_j and χ_j for $j = 1$ to $j = N-1$ with the exception that ψ_M is maintained at unity. The relaxation procedure is then repeated so long as ε decreases. It is found that of the order of 10^2 relaxation steps are required for ε to reach a minimum. For the reference situation, this relaxation procedure reduces ε from 0.2 to 0.018.

D. Numerical solution: an issue and its resolution

The numerical method results in the surprising result (see Fig.9) that the χ_M prescribed by Eq.113 differs from the χ_M for which $\varepsilon \to 0$; this indicates that there is something wrong with Eq.113 as it only predicts the order of magnitude of χ_M but not the precise value. Resolving this puzzle demonstrates not just a numerical issue, but an interesting and important physical property. To understand this issue, we now invoke two simplifications. The first simplification is to replace cylindrical geometry by more easily understood Cartesian geometry so we temporarily consider the pair of coupled equations

$$\frac{\partial^2 \psi}{\partial \bar{x}^2} + a_1 \psi = b_1 \chi \tag{149}$$

$$\frac{\partial^2 \chi}{\partial \bar{x}^2} + a_2 \chi = b_2 \psi. \tag{150}$$

These equations have $\bar{x}$ replace $\bar{r}$ and would lead to Eq.74 if the fields behaved according to Eq.1.

The second simplification is to assume that a_1, a_2, and b_1 are all spatially uniform but $b_2 = b_2(\bar{x})$. We define $\bar{x} = 0$ as the mode conversion location and define b_{20} as the value of b_2 at this location. Thus, in the vicinity of the mode conversion location

$$b_2(\bar{x}) = b_{20} + b_2' \bar{x}. \tag{151}$$

Solving for χ in Eq.149 gives

$$\chi = \frac{1}{b_1}\left(\frac{\partial^2\psi}{\partial\bar{x}^2} + a_1\psi\right) \tag{152}$$

and substituting this into Eq.150 gives

$$\frac{\partial^4\psi}{\partial x^4} + (a_1+a_2)\frac{\partial^2\psi}{\partial x^2} + (a_1a_2 - b_1b_2(\bar{x}))\psi = 0. \tag{153}$$

We first attempt to solve Eq.153 using the WKB approximation, that is we replace $\partial/\partial x$ everywhere in this equation by $ik_x(x)$ to obtain

$$k_x^4(x) - (a_1+a_2)k_x^2(x) + (a_1a_2 - b_1b_2(\bar{x})) = 0. \tag{154}$$

Equation 154 is a quadratic equation in $k_x^2(x)$ having the two roots

$$k_x^2(x) = \frac{a_1+a_2 \pm \sqrt{(a_1+a_2)^2 - 4(a_1a_2 - b_1b_2(\bar{x}))}}{2}. \tag{155}$$

The two roots coalesce at some location where $(a_1+a_2)^2 - 4(a_1a_2 - b_1b_2(\bar{x})) = 0$ and we define the value of the coalesced root to be

$$k_{mc}^2 = \frac{a_1+a_2}{2}. \tag{156}$$

Since b_{20} is defined as the value of $b_2(x)$ where coalescence occurs, the condition $(a_1+a_2)^2 - 4(a_1a_2 - b_1b_{20}) = 0$ implies that

$$b_{20} = -\frac{(a_1-a_2)^2}{4b_1}. \tag{157}$$

To examine behavior in the mode conversion vicinity without invoking the WKB approximation (i.e., without replacing $\partial/\partial x$ by $ik_x(x)$), the wave equation Eq.153 is expressed as

$$\frac{\partial^4\psi}{\partial x^4} + (a_1+a_2)\frac{\partial^2\psi}{\partial x^2} + \left(a_1a_2 - b_1\left(b_{20} + b_2'\bar{x}\right)\right)\psi = 0. \tag{158}$$

From Eq.156 and Eq.157 it is seen that

$$a_1a_2 - b_1b_{20} = k_{mc}^4 \tag{159}$$

so Eq.153 becomes

$$\frac{\partial^4\psi}{\partial x^4} + 2k_{mc}^2\frac{\partial^2\psi}{\partial x^2} + \left(k_{mc}^4 - b_1b_2'\bar{x}\right)\psi = 0. \tag{160}$$

We now consider Eq.160 in the vicinity of the mode conversion location, i.e., we consider Eq. 160 in the region $|\bar{x}| \ll k_{mc}^4/|b_1 b_2'|$. In this region, Eq.160 reduces to

$$\frac{\partial^4 \psi}{\partial x^4} + 2k_{mc}^2 \frac{\partial^2 \psi}{\partial x^2} + k_{mc}^4 \psi = 0 \tag{161}$$

which is a *uniform plasma* equation that can also be expressed as

$$\left(\frac{\partial^2}{\partial x^2} + k_{mc}^2\right)\left(\frac{\partial^2 \psi}{\partial x^2} + k_{mc}^2 \psi\right) = 0. \tag{162}$$

The width of the region where this uniform plasma approximation is valid is inversely proportional to b_2' and so this width becomes infinite when $b_2' \to 0$, i.e., when the plasma becomes fully uniform. Equation 161 and its equivalent form Eq. 162 are fourth-order ordinary differential equations with the four linearly independent solutions

$$\psi = e^{\pm i k_{mc}\bar{x}} \text{ and } \bar{x}e^{\pm i k_{mc}\bar{x}}. \tag{163}$$

To see why $\bar{x}e^{\pm i k_{mc}\bar{x}}$ is a valid solution to Eq.162, note that

$$\left(\frac{\partial^2}{\partial x^2} + k_{mc}^2\right)\left(\bar{x}e^{\pm i k_{mc}\bar{x}}\right) = \pm 2ik_{mc}e^{\pm i k_{mc}\bar{x}} \tag{164}$$

so

$$\left(\frac{\partial^2}{\partial x^2} + k_{mc}^2\right)\left(\frac{\partial^2}{\partial x^2} + k_{mc}^2\right)\left(\bar{x}e^{\pm i k_{mc}\bar{x}}\right) = \pm 2ik_{mc}\left(\frac{\partial^2}{\partial x^2} + k_{mc}^2\right)e^{\pm i k_{mc}\bar{x}} = 0. \tag{165}$$

It must be emphasized that even though the plasma is non-uniform, the solution of Eq.153 in the vicinity of the mode conversion location is just the solution for a uniform plasma having parameters identical to those of the mode conversion location.

The solution $\bar{x}e^{\pm i k_{mc}\bar{x}}$ *violates* the prescription given by Eq.1, *yet is a valid solution* for Eqs.149 and 150 in a non-uniform plasma in the vicinity of the mode conversion location. The WKB assumption that $\partial/\partial x$ can be replaced everywhere by $ik_x(x)$ is inappropriate for Eq.162 because such a replacement only pertains to the $e^{\pm i k_{mc}\bar{x}}$ solution and does not work for the $\bar{x}e^{\pm i k_{mc}\bar{x}}$ solution.

Since ψ is presumed real and is set to unity at $\bar{x} = 0$, the general form of ψ in the region $|\bar{x}| \ll k_{mc}^4/|b_1 b_2'|$ is

$$\psi(\bar{x}) = \cos(k_{mc}\bar{x}) + H_1 \sin(k_{mc}\bar{x}) + H_2 \bar{x}\cos(k_{mc}\bar{x}) + H_3 \bar{x}\sin(k_{mc}\bar{x}) \tag{166}$$

where each term satisfies Eq.161 and $\psi(0) = 1$; here H_1, H_2, H_3 are constants. Equation 166 gives

$$\begin{aligned}\frac{\partial^2 \psi}{\partial x^2} \;=\; & -N_x^2 \cos(k_{mc}\bar{x}) - N_x^2 H_1 \sin(k_{mc}\bar{x}) \\ & -H_2\left(2k_{mc}\sin(k_{mc}\bar{x}) + \bar{x}k_{mc}^2\cos(k_{mc}\bar{x})\right) \\ & +H_3\left(2k_{mc}\cos(k_{mc}\bar{x}) - \bar{x}k_{mc}^2\sin(k_{mc}\bar{x})\right)\end{aligned} \tag{167}$$

so

$$\left(\frac{\partial^2 \psi}{\partial x^2}\right)_{\bar{x}=0} = -k_{mc}^2 + 2H_3 k_{mc} \tag{168}$$

in which case

$$\chi(0) = \frac{1}{b_1}\left(-k_{mc}^2 + 2H_3 k_{mc} + a_1\right). \tag{169}$$

Using Eq.156 gives

$$\chi(0) = \frac{1}{b_1}\left(\frac{a_1 - a_2}{2} + 2H_3 k_{mc}\right). \tag{170}$$

If $H_3 = 0$, then Eq.170 reverts to Eq.113 since $2b_{20}/(a_2 - a_1) = (a_1 - a_2)/2b_1$ as indicated by Eq.157.

The numerical solution initially invoked Eq.113 which is a consequence of assuming solutions to equations analogous to $\left(\frac{\partial^2}{\partial x^2} + k_{mc}^2\right)\chi = 0$ and $\left(\frac{\partial^2}{\partial x^2} + k_{mc}^2\right)\psi = 0$. This invocation of Eq.113 thus failed to take into account the $\bar{x}e^{\pm ik_{mc}\bar{x}}$ solution that exists in the region $|\bar{x}| \ll k_{mc}^4/|b_1 b_2'|$. Thus, the assumption that Eqs.108 and 109 provide a complete description of the problem is incorrect because these equations do not predict $\bar{x}e^{\pm ik_{mc}\bar{x}}$ type of solutions. Because Eq.113 is derived from Eqs.108 and 109 which have been shown to provide an insufficient description, it is inferred that Eq.113 also provides an insufficient description and so cannot predict the value of χ_M that minimizes ε.

XI. VARIATION OF ρ_{mc} AND VARIATION OF $\bar{\omega}$

The previous section considered the reference situation where $\rho_{mc} = 6$ and $\bar{\omega} = 0.25$. This section will consider the effect of changing these parameters. Situations two and three involve having the mode conversion occurring at values of ρ_{mc} that are respectively larger and smaller than for the reference situation and so g at the mode conversion location will be respectively larger and smaller than for the reference situation (see Fig.2). Since ${N_z}^2 = 4g(\bar{r}_{mc})$ if displacement current is neglected, this means that the values of ${N_z}^2$ for situations two and three will be respectively larger and smaller than for the reference situation. Note that ${N_z}^2$ is precisely defined by Eq. 117 (displacement current included) and approximately defined by Eq.120 (displacement current ignored); the ${N_z}^2$ values in Fig.2 are calculated using Eq. 117.

Figure 10 plots ψ and χ for situation two which has $\rho_{mc} = 7$ while Fig 11 plots ψ and χ for situation three which has $\rho_{mc} = 5$.

These situation two and three plots show that ${N_z}^2$ changes in accordance with the prediction that ${N_z}^2 = 4g(\bar{r}_{mc})$ (to the extent that displacement current is neglected). Thus, situation two has

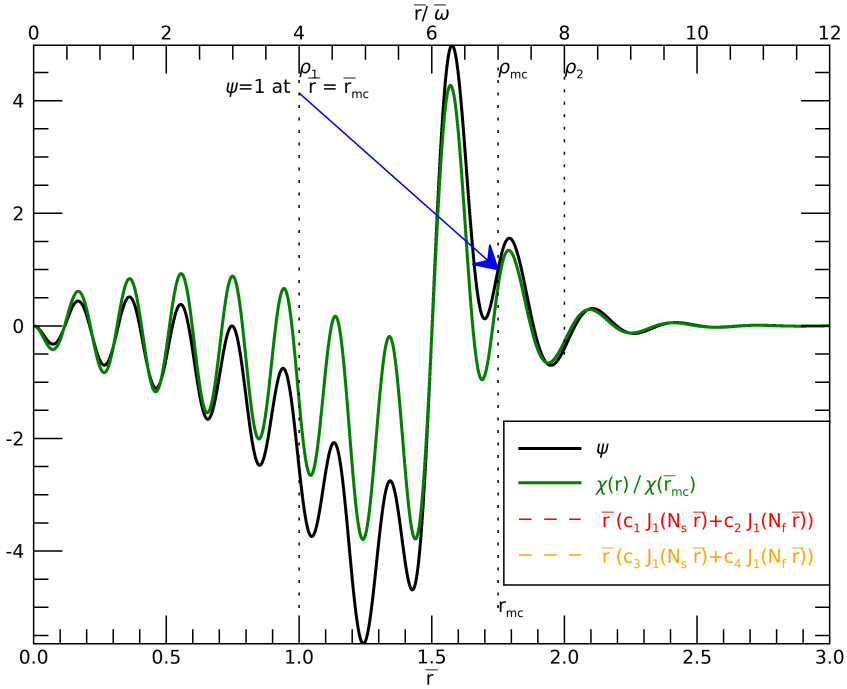

FIG. 10. Plot of ψ and χ for situation two ($\bar{\omega} = 0.25$ and $\rho_{mc} = 7$). Here there is larger difference between the wavelengths of the fast and slow modes compared to the reference situation.

a larger N_z^2 than the reference situation while situation three has a smaller N_z^2 than the reference situation. Since N_z^2 is the same for all $\bar{r}$, N_z^2 will also be larger in the uniform plasma region $\bar{r} < \bar{\omega}\rho_1$ than the N_z^2 of the reference case. Increase of N_z^2 corresponds to moving the vertical dashed line in Fig.1 to the right so the two interception points of this dashed line with the fast mode and slow mode parts of the $g = 25$ curve will move to the right. Thus increasing N_z^2 has the dual effect of reducing the value of N_r^2 for the fast mode (lower part of $g = 25$ curve) and increasing the value of N_r^2 for the slow mode (upper part of the $g = 25$ curve). Thus, compared to the reference situation, situation two will have a longer wavelength fast mode and a shorter wavelength slow mode in the uniform plasma region $\bar{r} < \bar{\omega}\rho_1$. In a similar fashion, situation three

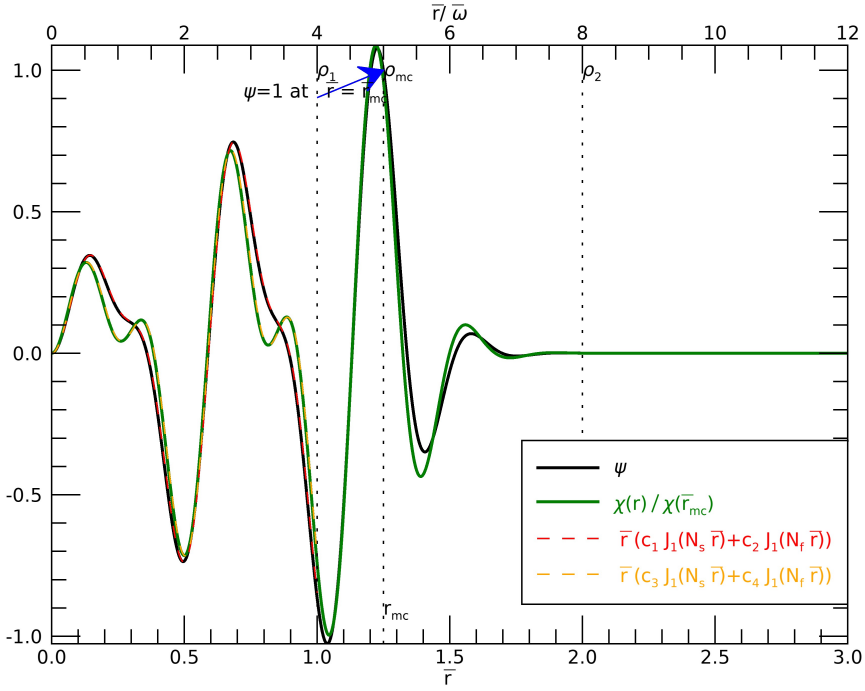

FIG. 11. Plot of ψ and χ for situation three ($\bar{\omega} = 0.25$ and $\rho_{mc} = 5$). Here there is a smaller difference between the wavelengths of the fast and slow modes compared to the reference situation.

has a smaller ${N_z}^2$ than the reference situation and so situation three has a shorter wavelength fast mode and a longer wavelength slow mode than the reference situation so situation three has much less difference between the wavelengths of the fast and slow modes.

This comparison of the reference situation with situations two and three can equivalently be interpreted as providing the dependence on ${N_z}^2$ for fixed $\bar{\omega}$. The interpretation is that so long as $4\min(g(\bar{r})) < {N_z}^2 < 4\max(g(\bar{r}))$ there will be a mode conversion at a location where ${N_z}^2 = 4g(\bar{r})$ and larger values of ${N_z}^2$ will have a greater difference between the wavelengths of the fast and slow mode in the low density interior of the duct.

Situation four has the same value of ρ_{mc} as the reference situation but has $\bar{\omega} = 0.20$ instead

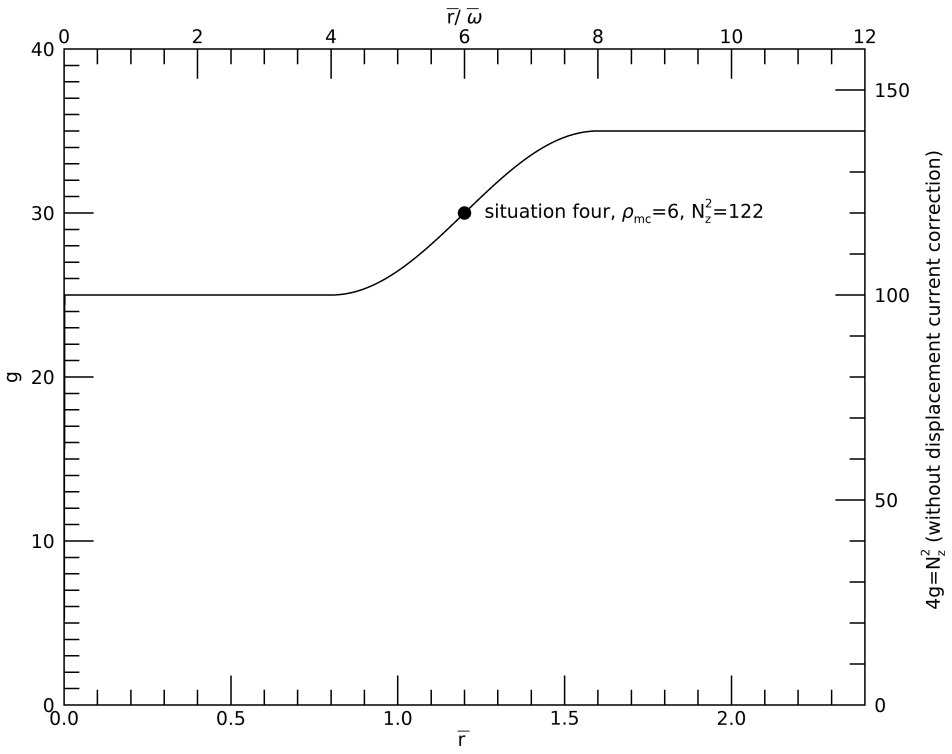

FIG. 12. Plot of g for situation four ($\bar{\omega} = 0.20$ and $\rho_{mc} = 6$). Compare to Fig.2 and note the difference in the scale of the frequency-dependent $\bar{r}$ axis but not in the scale of the frequency-independent $\bar{r}/\bar{\omega}$ axis.

of $\bar{\omega} = 0.25$ of the reference situation. The change in frequency has the effect of redefining $g(\bar{r})$ as shown in Fig. 12 so $\bar{r}_{mc} = 1.2$ now compared to 1.5 for the reference situation. Since actual distance is measured in terms of $r|\omega_{ce}|/c = \bar{r}/\bar{\omega}$ rather than in terms of the frequency-dependent $\bar{r}$, it is critical to plot ψ and χ as functions of $r|\omega_{ce}|/c = \bar{r}/\bar{\omega}$. Figure 13 plots ψ and χ using the same $r|\omega_{ce}|/c = \bar{r}/\bar{\omega}$ scale as in Fig.4 and comparison of these two figures shows that the wave profiles differ even though they have the same $N_z^2 = 4g$ at the mode conversion location (displacement current ignored).

However, because Eqs.90-92 depend on $\bar{\omega}$, the values of S, D, and P for situation four differ from the corresponding values for the reference situation. The fact that situation four and the ref-

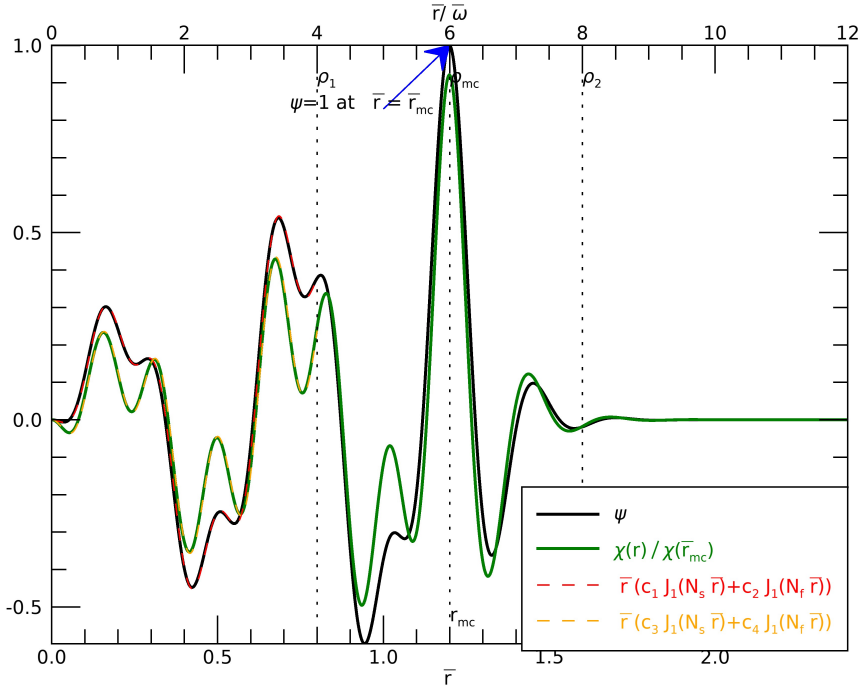

FIG. 13. Same as Fig.4, except $\bar{\omega} = 0.20$. Note that the plots of ψ and χ differ from the corresponding plots in Fig.4 even though Nz^2 is the same.

erence situation have the same N_z^2 but different frequencies might lead to the naive and erroneous conclusion that the system is non-dispersive, i.e., has behavior independent of frequency. In fact, the system is dispersive because the reference situation and situation four have different radial wavelengths. Comparison of Fig.14 with Fig.3 shows this difference. These differences show a dependence of the wave behavior on $\bar{\omega}$ even though N_z^2 does not depend on $\bar{\omega}$; thus the wave is dispersive despite N_z^2 being 'non-dispersive'.

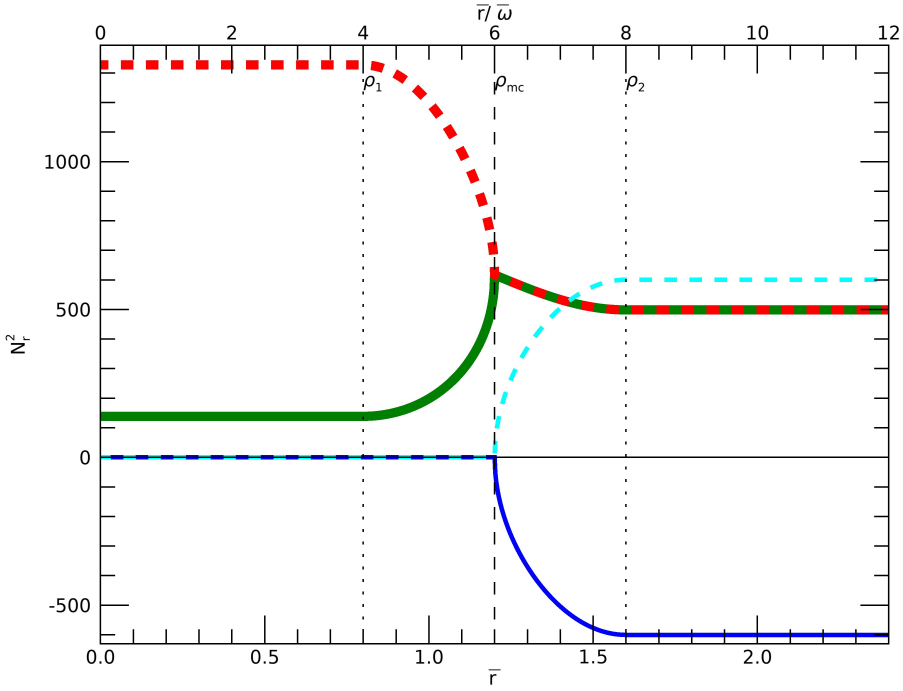

FIG. 14. Plot of $N_r{}^2$ for situation four ($\bar{\omega} = 0.20$ and $\rho_{mc} = 6$); Compare to Fig.3 and note the fast and slow roots of $N_r{}^2$ are larger in situation four than in the reference situation even though both situations four and the reference situation have the same $N_z{}^2$.

XII. CONCLUSION

We have shown that the coupled equations describing whistler propagation in a density duct can be solved numerically subject to the constraints that the poloidal wave flux ψ and the poloidal wave electric current χ are both real, that both scale as $\bar{r}^2$ near $\bar{r} = 0$ and that both decay exponentially at large $\bar{r}$ in the region outside the duct. Satisfying these constraints shows that the solution is physically realizable. Furthermore, the condition that both ψ and χ are pure real indicates that there is no power flow in the radial direction, whereas there is axial and azimuthal power flow.

These properties show the existence of a wave guided along the duct with no radial power leakage. The ψ and χ solutions in a uniform density region inside the duct are each the sum of two Bessel functions where one Bessel function is a standing slow wave and the other Bessel function is a standing fast wave. The ψ and χ solutions in the uniform density region outside the duct are decaying spatially oscillating standing waves having a single radial wavelength intermediate between the fast and slow wavelengths in the duct. The phase of the χ spatially decaying standing wave slightly leads the phase of the ψ spatially decaying standing wave. The rate of decay in the region outside the duct is large so these waves decay to infinitesimal amplitude in a radial distance of the order of the duct radius. The classic plane wave assumption prescribed by Eq.1 fails in the vicinity of the mode conversion location as there exists a previously ignored solution that in Cartesian coordinates has an $\bar{x}e^{\pm iN_x\bar{x}}$ dependence.

We have shown that the wave behavior depends on the location of the mode conversion location (which is equivalent to a dependence on ${N_z}^2$) and also on the wave frequency. Furthermore, situations having the same ${N_z}^2$ but different $\bar{\omega}$ will have different radial wavelengths. This dispersive behavior of the wave can be seen by dividing Eqs.6 and 7 by $\bar{\omega}^2$ which shows that changing $\bar{\omega}$ will change ${N_r}^2$ even if ${N_z}^2$ is kept constant. This change is such that both fast and slow waves have a larger ${N_r}^2$ when $\bar{\omega}$ is decreased.

We note that, as shown by Bakharev et al.[15], a situation could occur with appropriate density profile where the situation shown in Fig.3 is generalized to having a region of finite radial extent where real values of N_r^2 are located between inner and outer regions having complex conjugate values of N_r^2 in which case there would be a surface mode effectively trapped between a pair of mode conversion locations at two different radii.

We also note that if the plasma parameters have a gentle non-uniformity in the z direction, then N_z would have a gentle variation according to a WKB prescription. Similarly, collisions or Landau damping would cause attenuation but this would be extremely weak as whistler waves are observed to bounce along a duct from hemisphere to hemisphere several times with little attenuation as shown in the twelve-bounce train in Fig.7 of Storey[5].

ACKNOWLEDGMENTS

Supported by NSF Award Number 2403814.

REFERENCES

[1]T. H. Stix, *Waves in Plasma* (American Institute of Physics, New York, 1992).

[2]D. G. Swanson, *Plasma Waves* (Institute of Physics Publishing, Bristol, UK, 2003).

[3]P. M. Bellan, *Fundamentals of Plasma Physics* (Cambridge University Press, Cambridge, 2006).

[4]V. H. Barkhausen, "Zwei mit Hilfe der neuen Verstärker entdeckte Erscheinungen." Physik. Zeitschr. **XX**, 401 (1919).

[5]L. Storey, "An investigation of whistling atmospherics," Philosophical Transactions of the Royal Society of London. Series A, Mathematical and Physical Sciences **246**, 113–141 (1953).

[6]R. Gendrin, "Le guidage des whistlers par le champ magnetique," Planetary and Space Science **5**, 274–282 (1961).

[7]M. Laird and D. Nunn, "Full-wave VLF modes in a cylindrically symmetric enhancement of plasma density," Planetary and Space Science **23**, 1649–1657 (1975).

[8]D. L. Pasmanik and V. Y. Trakhtengerts, "Dispersion properties of ducted whistlers, generated by lightning discharge," Annales Geophysicae **23**, 1433–1439 (2005).

[9]A. V. Streltsov, M. Lampe, W. Manheimer, G. Ganguli, and G. Joyce, "Whistler propagation in inhomogeneous plasma," Journal of Geophysical Research: Space Physics **111**, 2005JA011357 (2006).

[10]A. V. Streltsov, J. Woodroffe, W. Gekelman, and P. Pribyl, "Modeling the propagation of whistler-mode waves in the presence of field-aligned density irregularities," Physics of Plasmas **19**, 052104 (2012).

[11]S. A. Nejad and A. V. Streltsov, "Switching Between Whistler-Mode Waves on Inhomogeneities of the Plasma Density and Magnetic Field," Journal of Geophysical Research: Space Physics **129**, e2024JA032442 (2024).

[12]V. I. Karpman and R. N. Kaufman, "Whistler wave propagation in density ducts," Journal of Plasma Physics **27**, 225–238 (1982).

[13]R. L. Stenzel, "Self-Ducting of Large-Amplitude Whistler Waves," Physical Review Letters **35**, 574–577 (1975).

[14]A. V. Kostrov, A. V. Kudrin, L. E. Kurina, G. A. Luchinin, A. A. Shaykin, and T. M. Zaboronkova, "Whistlers in Thermally Generated Ducts with Enhanced Plasma Density: Excitation and Propagation," Physica Scripta **62**, 51–65 (2000).

[15]P. V. Bakharev, T. M. Zaboronkova, A. V. Kudrin, and C. Krafft, "Whistler waves guided by

density depletion ducts in a magnetoplasma," Plasma Physics Reports **36**, 919–930 (2010).

[16]A. V. Kudrin, P. V. Bakharev, T. M. Zaboronkova, and C. Krafft, "Whistler eigenmodes of magnetic flux tubes in a magnetoplasma," Plasma Physics and Controlled Fusion **53**, 065005 (2011).

[17]N. Nassiri-Mofakham, "Whistler wave propagation in field-aligned density duct plasma," EPL (Europhysics Letters) **82**, 35001 (2008).

[18]I. Yu. Zudin, T. M. Zaboronkova, M. E. Gushchin, S. V. Korobkov, and C. Krafft, "Properties of Whistler Waves' Ducting in Plasmas With Systems of Small-Scale Density Depletions," Journal of Geophysical Research: Space Physics **128** (2023), 10.1029/2023ja031616.

[19]S. Cho, "Theory of mode conversion in helicon plasmas," Plasma Sources Science and Technology **29**, 095023 (2020).

[20]S. A. Nejad and A. V. Streltsov, "Whistler-Mode Waves on Density and Magnetic Shelves," Journal of Geophysical Research: Space Physics **129**, e2024JA032725 (2024).

[21]J. E. Maggs, G. J. Morales, and W. Gekelman, "Laboratory studies of field-aligned density striations and their relationship to auroral processes," Physics of Plasmas **4**, 1881–1888 (1997).

[22]R. Miteva and G. Mann, "The electron acceleration at shock waves in the solar corona," Astronomy & Astrophysics **474**, 617–625 (2007).

[23]Y. Tong, I. Y. Vasko, A. V. Artemyev, S. D. Bale, and F. S. Mozer, "Statistical Study of Whistler Waves in the Solar Wind at 1 au," The Astrophysical Journal **878**, 41 (2019).

[24]O. P. Verkhoglyadova, B. T. Tsurutani, and G. S. Lakhina, "Properties of obliquely propagating chorus," Journal of Geophysical Research: Space Physics **115**, 2009JA014809 (2010).

[25]S. T. Loi, T. Murphy, I. H. Cairns, F. W. Menk, C. L. Waters, P. J. Erickson, C. M. Trott, N. Hurley-Walker, J. Morgan, E. Lenc, A. R. Offringa, M. E. Bell, R. D. Ekers, B. M. Gaensler, C. J. Lonsdale, L. Feng, P. J. Hancock, D. L. Kaplan, G. Bernardi, J. D. Bowman, F. Briggs, R. J. Cappallo, A. A. Deshpande, L. J. Greenhill, B. J. Hazelton, M. Johnston-Hollitt, S. R. McWhirter, D. A. Mitchell, M. F. Morales, E. Morgan, D. Oberoi, S. M. Ord, T. Prabu, N. U. Shankar, K. S. Srivani, R. Subrahmanyan, S. J. Tingay, R. B. Wayth, R. L. Webster, A. Williams, and C. L. Williams, "Real-time imaging of density ducts between the plasmasphere and ionosphere," Geophysical Research Letters **42**, 3707–3714 (2015).

[26]J. D. Huba and H.-L. Liu, "Modeling the Development of Plasmasphere Ducts and Irregularities With SAMI3/WACCM-X," Geophysical Research Letters **50** (2023), 10.1029/2023gl105470.

[27]V. Harid, O. Agapitov, R. Khatun-E-Zannat, M. Gołkowski, and P. Hosseini, "Complex

Whistler-Mode Wave Features Created by a High Density Plasma Duct in the Magnetosphere," Journal of Geophysical Research: Space Physics **129**, e2023JA032047 (2024).

[28]W. Gu, X. Liu, Z. Xia, and L. Chen, "Statistical Study on Small-Scale ($\leq$1,000 km) Density Irregularities in the Inner Magnetosphere," Journal of Geophysical Research: Space Physics **127** (2022), 10.1029/2022ja030574.

[29]H. R. Lewis and P. M. Bellan, "Physical constraints on the coefficients of Fourier expansions in cylindrical coordinates," Journal of Mathematical Physics **31**, 2592–2596 (1990).

[30]R. L. Stenzel, "Whistler wave propagation in a large magnetoplasma," The Physics of Fluids **19**, 857–864 (1976).

[31]R. L. Stenzel and J. M. Urrutia, "Helicons in Unbounded Plasmas," Physical Review Letters **114**, 205005 (2015).

[32]R. A. Helliwell, "The role of the Gendrin mode of VLF propagation in the generation of magnetospheric emissions," Geophysical Research Letters **22**, 2095–2098 (1995).

[33]J. M. Urrutia and R. L. Stenzel, "Magnetic antenna excitation of whistler modes. III. Group and phase velocities of wave packets," Physics of Plasmas **22**, 072109 (2015).

[34]J. D. Jackson, *Classical Electrodynamics*, 3rd ed. (Wiley, 1999).

[35]P. M. Bellan, "Improved basis set for low frequency plasma waves," Journal of Geophysical Research-Space Physics **117** (2012).

[36]P. M. Bellan, "Alfvén 'resonance' reconsidered: Exact equations for wave propagation across a cold inhomogeneous plasma," Physics of Plasmas **1**, 3523–3541 (1994).

[37]S. Puri and M. Tutter, "Accessibility to the Lower Hybrid Resonance," Zeitschrift für Naturforschung A **28**, 438–442 (1973).

[38]P. M. Bellan, "An effective numerical method for linear mode conversion problems," Journal of Computational Physics **136**, 654–659 (1997).

[39]W. H. Press, S. A. Teukolsky, W. T. Vetterling, and B. P. Flannery, *Numerical Recipes*, 3rd ed. (Cambridge University Press, 2007).